A STUDY OF MICROFLUIDIC RECONFIGURATION MECHANISMS ENABLED BY FUNCTIONALIZED DISPERSIONS OF COLLOIDAL MATERIAL FOR RADIO FREQUENCY APPLICATIONS

A Thesis

by

SEAN ARTHUR GOLDBERGER

Submitted to the Office of Graduate Studies of
Texas A&M University
in partial fulfillment of the requirements for the degree of

MASTER OF SCIENCE

May 2009

Major Subject: Electrical Engineering

A STUDY OF MICROFLUIDIC RECONFIGURATION MECHANISMS ENABLED BY FUNCTIONALIZED DISPERSIONS OF COLLOIDAL MATERIAL FOR RADIO FREQUENCY APPLICATIONS

A Thesis

by

SEAN ARTHUR GOLDBERGER

Submitted to the Office of Graduate Studies of
Texas A&M University
in partial fulfillment of the requirements for the degree of

MASTER OF SCIENCE

Approved by:

Chair of Committee,	Gregory H. Huff
Committee Members,	Robert D. Nevels
	Kia Chang
	Richard Orville
Head of Department,	Costas N. Georghiades

May 2009

Major Subject: Electrical Engineering

ABSTRACT

A Study of Microfluidic Reconfiguration Mechanisms Enabled by Functionalized Dispersions of Colloidal Material for Radio Frequency Applications. (May 2009)

Sean Arthur Goldberger, B.S.E.E., University of Colorado

Chair of Advisory Committee: Dr. Gregory H. Huff

Communication and reconnaissance systems are requiring increasing flexibility concerning functionality and efficiency for multiband and broadband frequency applications. Circuit-based reconfiguration mechanisms continue to promote radio frequency (RF) application flexibility; however, increasing limitations have resulted in hindering performance. Therefore, the implementation of a "wireless" reconfiguration mechanism provides the required agility and amicability for microwave circuits and antennas without local overhead. The wireless reconfiguration mechanism in this thesis integrates dynamic, fluidic-based material systems to achieve electromagnetic agility and reduce the need for "wired" reconfiguration technologies. The dynamic material system component has become known as electromagnetically functionalized colloidal dispersions (EFCDs). In a microfluidic reconfiguration system, they provide electromagnetic agility by altering the colloidal volume fraction of EFCDs – their name highlights the special considerations we give to material systems in applied electromagnetics towards lowering loss and reducing system complexity.

Utilizing EFCDs at the RF device-level produced the first circuit-type integration of this reconfiguration system; this is identified as the coaxial stub microfluidic impedance transformer (COSMIX). The COSMIX is a small hollowed segment of transmission line with results showing a full reactive loop (capacitive to inductive tuning) around the Smith chart over a 1.2 GHz bandwidth. A second microfluidic application demonstrates a novel antenna reconfiguration mechanism for a 3 GHz microstrip patch antenna. Results showed a 300 MHz downward frequency shift by dielectric colloidal dispersions. Magnetic material produced a 40 MHz frequency shift. The final application demonstrates the dynamically altering microfluidic system for a 3 GHz 1x2 array of linearly polarized microstrip patch antennas. The parallel microfluidic capillaries were imbedded in polydimethylsiloxane (PDMS). Both E- and H-plane designs showed a 250 MHz frequency shift by dielectric colloidal dispersions. Results showed a strong correlation between decreasing electrical length of the elements and an increase of the volume fraction, causing frequency to decrease and mutual coupling to increase. Measured, modeled, and analytical results for impedance, voltage standing wave ratio (VSWR), and radiation behavior (where applicable) are provided.

DEDICATION

This thesis is dedicated to my parents, grandparents, and sister.

ACKNOWLEDGEMENTS

I would like to thank my committee chair, Dr. Gregory Huff, and my committee members, Dr. Robert Nevels, Dr. Kia Chang, and Dr. Richard Orville, for their guidance and support throughout the course of this research.

Thanks also go to my friends and colleagues and the Electrical and Computer Engineering department faculty and staff for making my time at Texas A&M University a great experience.

I would like to thank Fermag Technologies, Inc. for supplying the Ferrite Powder #UHE 14 used in the microstrip patch experiments.

A special thanks to my students from the Space Engineering Institute, Rachel Angelina Anderson, Joel Barrera, Amy Bolon, Stephen Davis, Jamie Edelen, Justin Marshall, Cameron Peters, David Umana, and assistant mentor Frank Drummond for their assistance in preparation and execution of the experiments performed in this thesis.

Thanks to my mother, father, sister, and grandparents for their encouragement, patience, and love.

Finally, a thank you to my Father in heaven and His Son, my Lord and Savior for His unending love and for the talents He has graciously loaned to me.

NOMENCLATURE

EFCD	Electromagnetically Functionalized Colloidal Dispersions
BSTO	Barium Strontium Titanate
RF	Radio Frequency
EM	Electromagnetic
PDMS	Polydimethylsiloxane
VSWR	Voltage Standing Wave Ratio
SOA	State-of-the-Art
CPW	Coplanar Waveguide
COSMIX	Coaxial Stub Microfluidic Impedance Transformer
ϑ	Volume Fraction
TEM	Transverse Electromagnetic
TM	Transverse Magnetic
MIMO	Multiple Input and Multiple Output
MEMS	Micro Electromechanical System
s_{eff}	Universal effective material properties
s_1	Universal liquid material properties
s_2	Universal colloid material properties
s_i	Universal inclusion material
s_e	Universal environment material
DC	Direct Current
PIN	Positive Intrinsic Negative

TABLE OF CONTENTS

CHAPTER Page

LIST OF FIGURES

FIGURE Page

FIGURE Page

CHAPTER I

INTRODUCTION

Advances in radio frequency (RF) technological requirements have increased the demand for adaptive systems in national defense, communications, finance/banking, security, and imbedded RF technologies. Many communication and reconnaissance systems must operate continuously under harsh environmental and electromagnetic conditions. These vital systems require increased flexibility, availability, reliability, maintainability, new degrees of multiband and broadband frequency functionality and operation efficiency. New technologies and operational paradigms must be developed that provide significant improvement for these demanding applications' electromagnetic agility. This research is being conducted on a candidate reconfiguration mechanism for these demanding applications.

Impedance matching, radiation behavior, and bandwidth are critical system operation constraints existing in RF circuit devices and antennas and have encouraged the developments of numerous reconfiguration mechanisms. Adaptive impedance matching circuits have been designed with state-of-the-art (SOA) components [1-4] (e.g., RF MEMS and reactive computer controlled switches) that play key roles in many of these designs. Frequency, radiation, and polarization reconfiguration of antennas have also been implemented with SOA components [5-10] (e.g., PIN diodes, RF MEMS, and photoconducting switches). However, the application of SOA components has increased

---

This thesis follows the style of *IEEE Transactions on Antennas and Propagation*.

overall system/fabrication complexity in large-scale implementations and sometimes places a burden on system resources through spatial constraints, bias/control circuitry, and power consumption (depending on the design complexity). These limitations can hinder the performance and practicality of reconfigurable RF devices. This motivates the following thesis statement for this work.

A pressure driven vascular network of functionalized colloidal dispersions provide a significant improvement in performance versus complexity over 'wired' SOA reconfiguration mechanisms and substantially increase the electromagnetic agility in microwave circuits and antennas.

The "wireless" reconfiguration mechanism examined through this research integrates a dynamic and fluidic-based material system to facilitate electromagnetic agility and reduce the need for "wired" reconfiguration technologies (where "wired" refers to a device with input, output, bias, and control terminals by which electrical signals are delivered to a device that alters the device-level EM characteristics). This fluidic-based system contains electrostatically-stabilized dispersions of magnetodielectric colloidal nanoparticles in a low-loss non-aqueous liquid - referred to as electromagnetically functionalized colloidal dispersions (EFCDs). These are transported within a fluidic network and represent the basis for a novel reconfiguration technology in antennas and circuits. Dynamic material systems facilitate electromagnetic agility [11-17] by altering the volume fraction of colloids and EFCD position within a given topology to reversibly alter RF device performance. The dynamic pressure-driven

flow and displacement of EFCDs within a fluidic system is analogous to the flow of blood cells and other materials in the human circulatory system.

The objective, accomplished through altering electromagnetic visibility via transport and displacement in a microfluidic reconfiguration mechanism, remains to diminish loss mechanisms without affecting the desired operation by removing the need for conductive biasing and/or control lines often in close proximity to the RF device (e.g., antenna, circuits, etc.). This differs substantially from prior technologies and investigations on similar devices [18-19] and tuning mechanisms [20-23].

This thesis begins with several topics necessary for comprehensive understanding of microfluidic reconfiguration including a broad overview of state-of-the-art antenna and circuit reconfiguration techniques, a review of colloidal dispersions, material preparations, and microstrip patch antenna theory to provide a foundational analysis of design techniques used in this work. The design and analysis of a coaxial stub microfluidic impedance transformer (COSMIX) with an emphasis on transmission line theory and representation of the microfluidic capillaries. The COSMIX is a small hollowed segment of transmission line with results showing a full reactive loop (capacitive to inductive tuning) around the Smith chart over a 1.2 GHz bandwidth. A second microfluidic application demonstrates a novel antenna reconfiguration mechanism for 3 GHz microstrip patch antenna. Results showed a 300 MHz downward frequency shift by dielectric colloidal dispersions. Highly magnetic material produced a 1 GHz frequency shift. The final application demonstrates the dynamically altering microfluidic system for a 3 GHz 1x2 array of linearly polarized microstrip patch

antennas. The parallel microfluidic capillaries were imbedded in Sylgard 184 [24]. Both E- and H-plane cases were examined. Results showed a strong correlation between decreasing electrical length of the elements and an increase of the volume fraction, causing frequency to decrease and mutual coupling to increase. Measured, modeled, and analytical results for impedance, VSWR, and radiation behavior (where applicable) are provided. The thesis concludes with a summary of work accomplished and future research.

CHAPTER II

BACKGROUND

A. An Overview of Antenna Reconfiguration Mechanisms

Reconfiguration has been implemented through integrated circuitry, optics, and physical antenna deformation. Frequency, radiation pattern, and polarization reconfiguration are three different approaches available for adapting antenna parameters to any reconfigurable application (e.g., multiple input and multiple output systems (MIMO), telecommunications, radar, spread spectrum communications, remote sensing and imaging, electronic intelligence, etc.). Cost, shape, and size of reconfigurable antennas encourages their attraction to commercial, government, educational, and private citizen purchase. PIN diodes, photoconducting switches, RF MEMS, and varactors represent some SOA components available for enhancing antennas.

PIN diode size range varies from 200 μm to 2 mm and is applied in pattern and frequency reconfigurable antenna applications [7, 9, 25]. PIN diodes are placed within the antenna structure to enhance performance. Additional circuit components are required to protect the RF generator, DC power supply, and diodes from each other. DC bias lines are surface mounted to the antenna or small wire leads connect the diodes to the power source. To limit the DC voltage across the diode, an optional resistor connects to each diode. In the presence of the RF fields, capacitors and inductors are installed. The capacitor provides a DC block protecting the RF generator. The inductor, in series with the diode, creates a RF choke protecting the DC generator.

Photoconducting switches are built with n-type silicon wafers doped with phosphorus [8]. These switches use photons for activation and bias wires or match circuits are required for operation. The phosphorus has a high density of free-floating electrons and electron holes. When photons strike the semi-conductor surface, the free-floating electrons and holes are excited and form a closed circuit. Absence of light forms an open circuit. The switch depends upon a light source activated and deactivated when needed and penetrates photons deep in the silicon wafer activating the doped phosphorus.

Unlike photoconducting switches, RF MEMS switches do not require custom manufacturing, but custom manufacturing remains available. RF MEMS [2, 5-6, 26-33] are made from silicon semi-conductors. A RF MEMs switch operates like field effect transistors, with a drain, gate, and source. Depending on manufacturing specifications when activated, the RF MEMS acts as a segment of transmission line and for an antenna this would be 50 Ω. In an inactive state, RF MEMS electrically respond as a large capacitor [30]. RF MEMS have other applications providing varying capacitance depending on the bias voltage.

Reverse biasing a varactor [34] causes operation as a variable capacitance. As the bias voltage increases, the capacitance decreases. Removing the bias voltage or forward biasing the varactor causes it to act as a short circuit. A varactor requires the same passive filter network as the PIN diode, providing isolation between the DC and RF signals.

B. Frequency Reconfigurable Antennas

Several designs have been published [8-9, 25, 31, 34-36] discussing a different methods of frequency reconfiguration. Frequency reconfiguration adjusts the antenna resonant frequency up or down the RF spectrum for pre-selected frequencies. Out of the several dozen or more designs available, five reconfiguration designs will be discussed using some of the SOA components described above.

The authors of [31] designed a frequency tunable patch antenna using RF MEMS. The design took a standard patch antenna at 16 GHz and added a coplanar waveguide (CPW) load. Five RF MEMS switches were designed to act as variable capacitors bridging the CPW gap. The five switches varied the reactive loading of the CPW by acted as capacitive stubs providing continuous tuning. Connecting the CPW to the patch radiating edge provided a variable load, increasing the effective antenna length lower the frequency, and resulting in a 300 MHz downward resonant frequency shift. The authors of [34] designed a varactor tunable antenna. One varactor was placed on each radiating edge. Bias varying the varactor controlled the resonant frequency. Increasing the bias voltage decreases the varactor capacitance and increases the frequency. Decreasing the voltage does the exact opposite. A 200 MHz frequency shift range was achieved.

Photoconducting diodes have been integrated into a monolithic dipole design [8]. These switches increase or decrease the dipole arm length and change the resonant frequency in one step from 3.15 GHz to 2.26 GHz. An annular slot antenna can be frequency and pattern reconfigurable depending on PIN diode placement [9]. The PIN

diodes create shorts in the antenna changing the frequency resonance and pattern orientation. Changing the resonance provided a 600 MHz variable frequency range.

C. Other Reconfigurable Antennas (Radiation and Polarization)

Several designs have been published [6, 8-9, 25, 30, 37-39] discussing a different methods of pattern and polarization reconfiguration. Pattern reconfiguration changes the antenna's radiating fields by changing beam direction or beam type (i.e., broadside and end-fire). Polarization reconfiguration alters the orientation of the electric field vector defining linear, circular, and elliptical polarizations. A few designs will be discussed using *SOA* components.

Three parallel microstrip lines combined with some generic switches created a pattern reconfigurable parasitic array [37]. The center microstrip line operated as a dipole. Turning the switches on or off determined the beams directional orientation. If the element to the left of the center dipole was longer and the element to the right was shorter than the center, then the left element would reflect and the right element would direct. A second example takes a square spiral and RF MEMS switches [30] to change the pattern from broadside to end-fire depending on switch activation and the spiral microstrip line section shorted or open. Finally, polarization reconfiguration with a circular microstrip patch antenna [38]. PIN diodes and a U-shaped slot are manipulated to change the polarization. With the diodes all on or off the antenna remains linearly polarized. With one diode on and the other off, creates right-hand-circular-polarization or left-hand-circular-polarization.

CHAPTER III

COLLOIDAL MATERIALS AND ANALYTICAL TECHNIQUES

A. General Description of Colloidal Dispersions

Colloidal particles are larger than molecules (diameter < 1 nm), but are small enough for dispersal in a fluid or plasma. Colloidal dispersions occur between suspensions and solutions. Mixing a small amount of sand in a glass of water produces a suspension and a heterogeneous mixture [40]. The human eye easily sees sand particles (diameter ~ 2000 μm) and distinguishes them from water molecules. Lemonade powder mixed in water produces a solution and a homogeneous mixture. The lemonade particles are distributed evenly in the water and appear to have dissolved completely. Different nomenclatures describe a colloidal dispersion depending on the constituent material phases (e.g. solid, liquid, and gas). This thesis focuses on the performance of solid-liquid dispersions known as "sols." Common examples of sols include blood, lemonade, and paint.

EFCDs are sols resulting from the homogeneous diphase dispersions of solid colloidal materials (spherical, magnetodielectric, low-loss particles with a diameter ranging from 1 to 1000 nm) in a low-loss non-aqueous liquid. The particle size and wavelength ratio determines homogeneity. When this ratio results in a number much smaller than unity, particle grouping (i.e., a magnetodielectric medium) appears homogeneous to the incident wave. If the particle size appears large with respect to the wavelength, scattering occurs and the particles become obstacles. For example, in the

Great Lakes region, airborne radar units measure snow depth to quantify water in gallons per acre for determining potential flooding or drought conditions. The radar wavelength is much greater than the diameter of an individual snowflake permitting the radar signal to pass through without Mie or resonant scattering. Therefore, the snow acts as a dielectric layer and seen as a homogeneous medium by the radar.

Magnetodielectric colloidal particles are selected for use in EFCDs and high frequency applications based on their ability to alter the local complex constitutive parameters (ε, μ) and provide varying degrees of electromagnetic flexibility with low losses. A mixing formula determines the complex constitutive parameters for the EFCDs. Fig. 1 shows a conceptual illustration of EFCDs and homogeneous mixing formulas (e.g., Maxwell Garnett formula (1) [41]) for a nominal set of materials flowing inside a capillary structure or fluid channel.

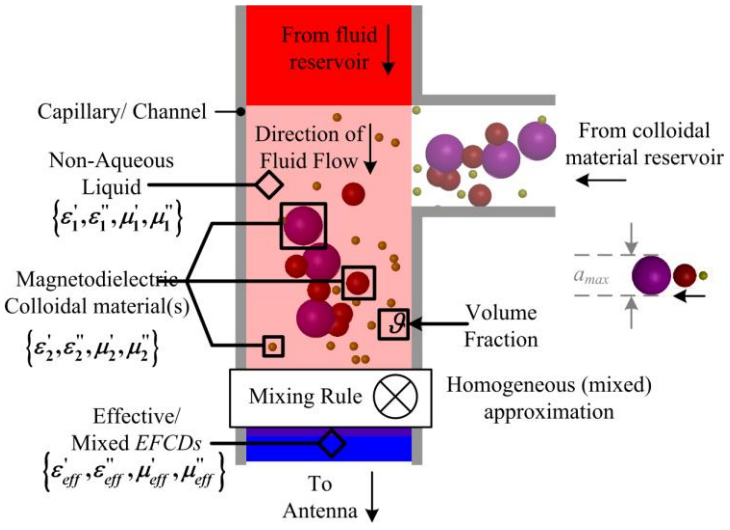

Fig. 1. The dynamic material system for colloids dispersed in a liquid (EFCDs) that are flowing down a capillary or fluid channel.

In 1904, J. C. Maxwell Garnett published in the Transactions of the Royal Society in London, an effective permittivity relationship between metal spheres suspended in a medium. This relationship became known as the Maxwell Garnett formula, ideal for non-polarized and randomly oriented particle dispersions (illustrated in Fig. 2). The effective constitutive EFCD material parameter s_{eff} resulting from mixing a liquid s_1 and a volume fraction ϑ of a colloidal material s_2 (assuming they are of uniform size and geometric shape) shown in (1); s in this expression captures the complex (lossy) properties because $s = s\left(1 - j\tan\delta\right)$ (s can be independently ε or μ).

$$s_{eff} = s_1 + 3s_1\vartheta\frac{s_2 - s_1}{s_1 + s_2 - \vartheta\left(s_2 - s_1\right)} \tag{1}$$

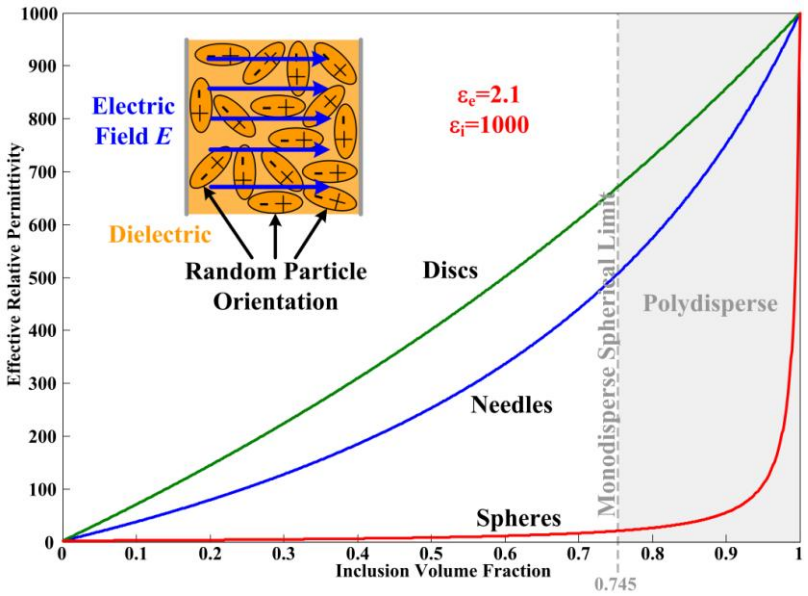

Fig. 2. Effective permittivity ε_{eff} calculated using the Maxwell Garnett mixing rule for mixtures of discs, needles, and spherical colloids having an inclusion permittivity ε_i = 1000 and environmental permittivity ε_e = 2.1.

Particle collections of spherical colloids possessing a uniform radius are called monodispersed. Fig. 3 (left) demonstrates a monodispersed system with glass marbles. For a monodispersed system, only so many marbles are packed into a designated volume like the beaker. Leaving air gaps between each marble in the beaker provides a maximum marble to air ϑ of 74.5%. To increase ϑ beyond the monodispersed spherical limit, the mixing formula needs to be extended to include heterogeneous materials, in order to produce polydispersed mixtures (particles with an inconsistent spherical radius), Fig. 3 (right). BB's were added to the mixture for reducing the air gaps between marbles resulting in a higher ϑ. Reducing air gaps between particles and increasing ϑ, increases particle clumping.

Fig.3. Photos demonstrating a monodispersed system of spherical particles using marbles (left) and polydispersed particles using a mixture of marbles and BB's (right).

Achieving high ϑ in a polydispersed environment would not be possible without a surfactant. Fig. 4 visualizes surfactant adding a second layer to each particle or double layer. Ionic dispersants, or surfactants, create an electrical double layer that electrostatically-stabilizes the colloids (e.g., coats them in like-charged, repulsive 'shell') to mitigate many of the inter-particle forces (Van der Waals, etc.) causing aggregation and clotting. This electrical double layer (created by the surfactant) produces a partially non-homogeneous particle (shown in Fig. 4). Analyzing the layered structure with the Maxwell Garnett rule, for multiple spherical particle layers (2) [41], solves the material properties for only two layers. The relationship between ϑ and the ratio of a_2/a_1 are provided in (3).

$$\frac{s_{eff}-s_e}{s_{eff}+2s_e}=\vartheta\frac{(s_1-s_e)(s_2+2s_1)+\frac{a_2^3}{a_1^3}(s_2-s_1)(s_e+2s_1)}{(s_1+2s_e)(s_2+2s_1)+2\frac{a_2^3}{a_1^3}(s_2-s_1)(s_1-s_e)} \tag{2}$$

$$\vartheta=\vartheta_1+\vartheta_2 \text{ and } a_2^3/a_1^3=\vartheta_1/(\vartheta_1+\vartheta_2) \tag{3}$$

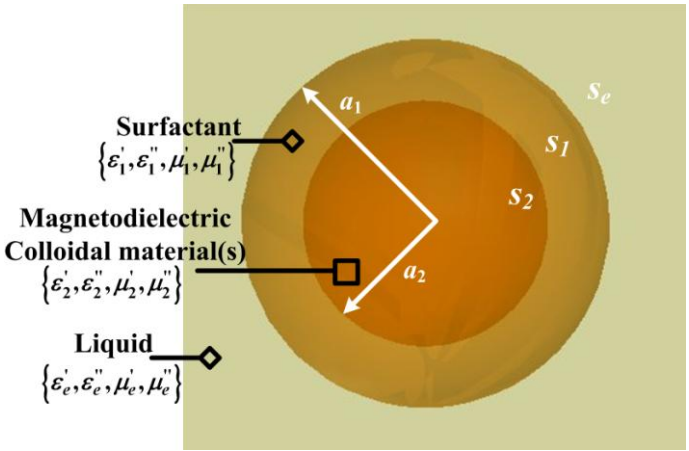

Fig. 4. A spherical particle s_2 coated by a surfactant s_1 dispersed in a liquid with s_e.

EFCDs are electromagnetically functionalized by considering the reduction of loss mechanisms, their ability to maintain low viscosities while using high permittivity and permeability colloidal material, and introducing particles of varying geometries. Colloidal shape influence electromagnetic visibility, another significant factor influencing EFCD performance. The Maxwell Garnett formula is adaptable for various ellipsoidal geometries [41]; (4) shows the effective material parameters for needle or whisker shaped particles and (5) for disk shaped particles. Fig. 2 illustrates both having the same environmental phase (i.e., liquid solvent) and inclusion phase (i.e., solid colloidal material) permittivities.

$$s_{eff} = s_e + \vartheta\left(s_i - s_e\right)\frac{s_i + 5s_e}{\left(3-2\vartheta\right)s_i + \left(3+2\vartheta\right)s_e} \tag{4}$$

$$s_{eff} = s_e + \vartheta\left(s_i - s_e\right)\frac{2s_i + s_e}{\left(3-\vartheta\right)s_i + \vartheta s_e} \tag{5}$$

Particle orientation and geometry influence electromagnetic visibility. Fig. 5 shows needles and disks have a minimum and maximum permittivity depending on their orientation. If the particles were manipulated so their maximum surface area is perpendicular to the direction of the electromagnetic field, then permittivity would be at a maximum. During a regatta, a sailboat races from buoy to buoy across a lake with the winner possessing the top buoy approach speed. To harness the wind, the sailboat hoists its' sail and points it a few degrees off the wind direction called pointing higher. The greater the sail's surface area, the more wind resistance, increasing velocity, and the faster the crew reaches the next buoy. If the sail were pointed away from the wind, the sail would be luffing or not "catching" the wind and causing it to flap like a flag. The

same principle applies to fighters taking off an aircraft carrier. Therefore, if the needles and disks are aligned so their minimum surface area remains parallel to the direction of the fields, then the permittivity remains a minimum.

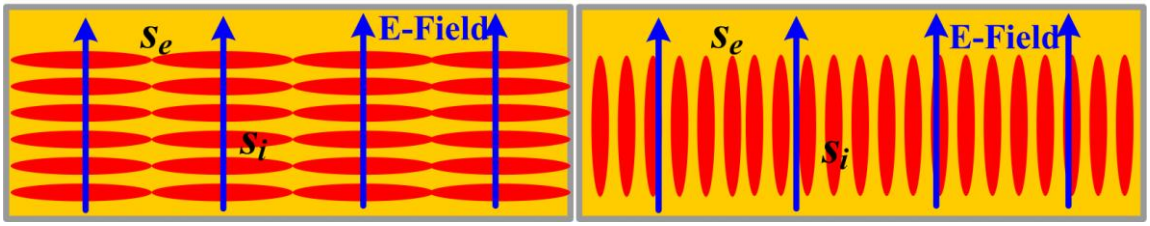

Fig. 5. Needle shaped particles "flared" in the presence of a traveling electromagnetic field (left). Needle particles and an electromagnetic field are mutually traveling in the same direction (right).

B. Material Preparation

Four components were used to create the EFCDs: a low-loss petroleum distillate [42], Barium Strontium Titanate (BSTO) [43], strontium hexaferrite [44], and Nanosperse ™ surfactant [45]. BSTO has a chemical composition of $Ba_xSr_{1-x}TiO_3$ with x (molar concentration) being 60:40 or 0.6 Barium and 0.4 Strontium. Fig. 6 (left) shows BSTO 60:40 spherical particles have varying radii less than 50nm and a polydispersed composition. Strontium hexaferrite ($SrFe_{12}O_{19}$) has a particle diameter of $0.2\mu m < a_{max} < 2\mu m$ shown at right of Fig. 6.

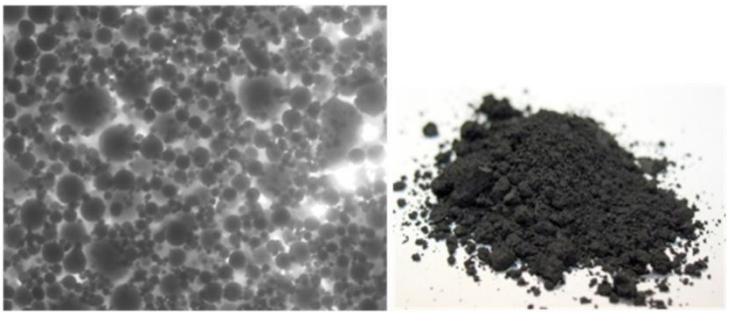

Fig. 6. Photos of 60:40 BSTO (left) and strontium hexaferrite (right).

Fig. 7 demonstrates the process of obtaining and preparing the EFCD ϑ combined with analytical chemistry. This process includes collecting the solids and solvents, obtaining mass measurements, and agitating components simultaneously. Calculating the $\vartheta(6)$ of colloidal particles entails knowing bulk density, mass, and distillate volume. The mass of material particles divided by the total volume they occupy define bulk density. The bulk densities of BSTO 60:40 and strontium hexaferrite are 1.5 g/cc and 1.0412 g/cc respectively. These mixtures were repeatedly vortexed (vigorously shaken and stirred) for 15 minutes and sonicated (degassed and sifted) for 30 minutes creating a homogeneous sol.

$$\vartheta = \text{Mass[g]} \Big/ \Big[\big(\text{Volume of Liquid [ml]}\big)\big(\text{Bulk Density[g/cc]}\big) + \text{Mass[g]} \Big] \qquad (6)$$

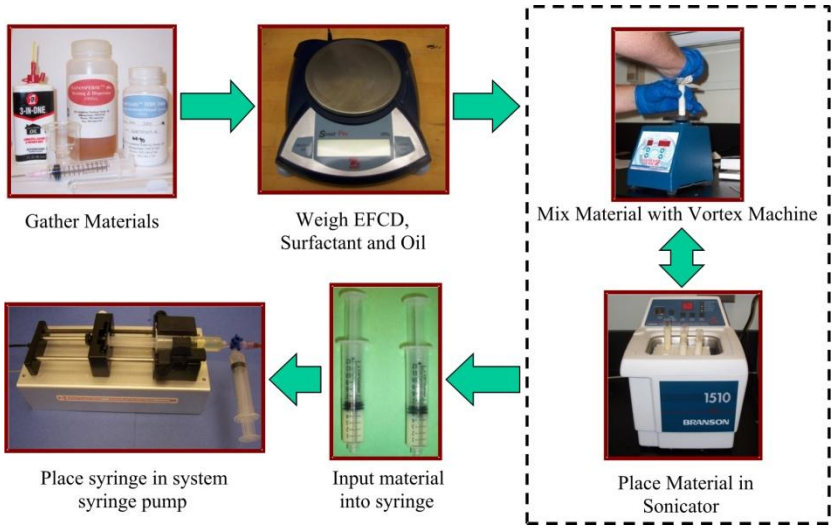

Fig. 7. Illustrates process for material preparation and characterization.

C. Theory and Operation of a Microstrip Patch Antenna

Microstrip antennas are inexpensive, have a low profile, and very geometrically. Important variable antenna qualities include resonant frequency, impedance, polarization, and radiation patterns. Fig. 8 illustrates a microstrip patch antenna and its critical parameters. The two-metallization layers and the substrate form a cavity producing an electromagnetic resonance. Patch length and substrate permittivity determines the dominate mode's resonant frequency in Fig. 9.

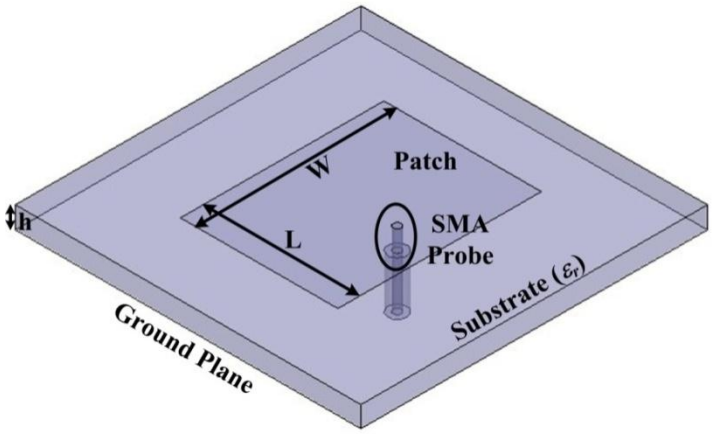

Fig. 8. Geometrical visualization and design parameters of a microstrip patch antenna.

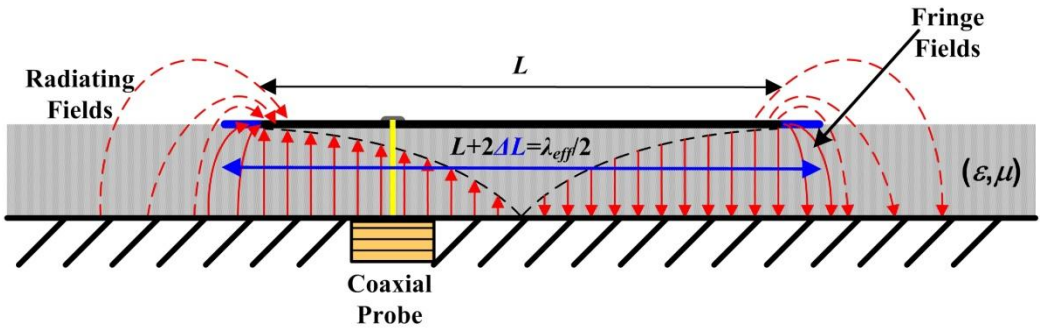

Fig. 9. Dominate mode representation of TM_{10} electric fields of the microstrip patch antenna.

The sinusoidal TM_{10} mode – has an electric field amplitude maximum at both edges, are 180^{o} out of phase (i.e. they point in opposite directions), and a sinusoidal half-period distribution in the cavity center. The coaxial probe couples electromagnetic energy exciting the dominate mode. Probe position determines the matched input impedance relative to the patch length. Mismatch results in standing waves and power loss. Fig. 9 illustrates the fringing fields extend outward, decreasing in strength, and

radiating from the slots or apertures. The 180° phase relationship and effective distance L_{eff} between apertures, determines the radiation pattern.

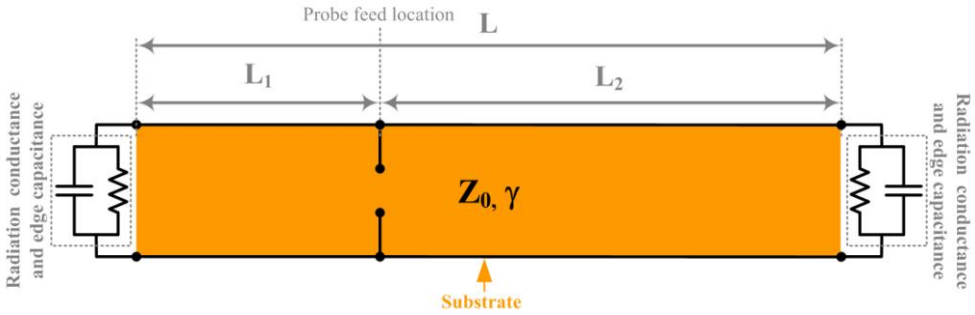

Fig. 10. Transmission line representation of a microstrip patch antenna.

Fig. 10 shows transmission line representation of the patch. Fig. 9 shows the patch length to be a half wavelength, which relates to the resonant frequency. The transmission line model (TLM) requires knowing the resonant frequency, substrate permittivity, and height. This allows design completion in four steps [56]: 1) Calculate the width (7) for efficient aperture radiation, 2) determine the effective dielectric constant (8), which accounts for field fringing, 3) calculate the length extension (9), ΔL, required to remove the complex impedance of the patch and accounts for the patch being electrically longer because of the field fringing seen in Fig. 9, and finally 4) calculate the physical length and effective length based on steps 1 – 3 and (10-11).

$$W = \frac{1}{2 f_0 \sqrt{\mu_0 \varepsilon_0}} \sqrt{\frac{2}{\varepsilon_r + 1}} \tag{7}$$

$$\varepsilon_{eff} = \frac{\varepsilon_r + 1}{2} + \frac{\varepsilon_r - 1}{2} \left[1 + 12 \frac{h}{W} \right]^{-1/2} \text{ for } \frac{W}{h} > 1 \tag{8}$$

$$\frac{\Delta L}{h} = 0.412(\varepsilon_{eff} + 0.3)\left(\frac{W}{h} + 0.264\right) \Big/ \left[(\varepsilon_{eff} - 0.258)\left(\frac{W}{h} + 0.8\right)\right] \tag{9}$$

$$L = 1 \Big/ \left(2 f_0 \sqrt{\varepsilon_{eff}}\sqrt{\mu_0 \varepsilon_0}\right) - 2\Delta L \tag{10}$$

$$L_{eff} = L + 2\Delta L \tag{11}$$

Increasing the permittivity and/or permeability inside the cavity increases the number of wavelengths (12) and causes the cavity to appear "electrically longer."

$$\lambda_{eff} = \frac{\lambda_0}{\sqrt{\varepsilon_{reff}\,\mu_{reff}}} \tag{12}$$

The antenna input impedance Z_A (13) determines the maximum power transfer from probe to antenna. If the antenna and Z_A are matched (typically 50 Ω) results in 100% power transmission. If a mismatch exists, some or all of the power will reflect at the probe and patch junction.

$$Z_A(f) = \frac{V_A(f)}{I_A(f)} = \frac{|V_A(f)|\angle\varphi_V^{\circ}}{|I_A(f)|\angle\varphi_I^{\circ}} = \mathrm{Re}(Z_A(f)) + j\,\mathrm{Im}(Z_A(f)) \tag{13}$$

The magnitude and phase of the input of scattering parameter S_{11} characterizes the impedance match (14-15). Any reflected power causes a standing wave, measured as a voltage-standing-wave-ratio (*VSWR*) (16).

$$S_{11} = \frac{Z_A - Z_o}{Z_A + Z_o} = \mathrm{Re}(S_{11}) + j\,\mathrm{Im}(S_{11}) = |S_{11}|e^{j\theta} \tag{14}$$

$$|S_{11}|^2 = (\text{Reflected Power}) \big/ (\text{Input Power}) \tag{15}$$

$$VSWR = \left(1 + |S_{11}|\right) \Big/ \left(1 - |S_{11}|\right) \tag{16}$$

An optimal VSWR means S_{11} = 0 and a VSWR of 2:1 indicates that 89% of power is delivered. In Fig. 11, where VSWR equals two, defines the operating bandwidth metric selected for this thesis and shows a resonant frequency of 3 GHz.

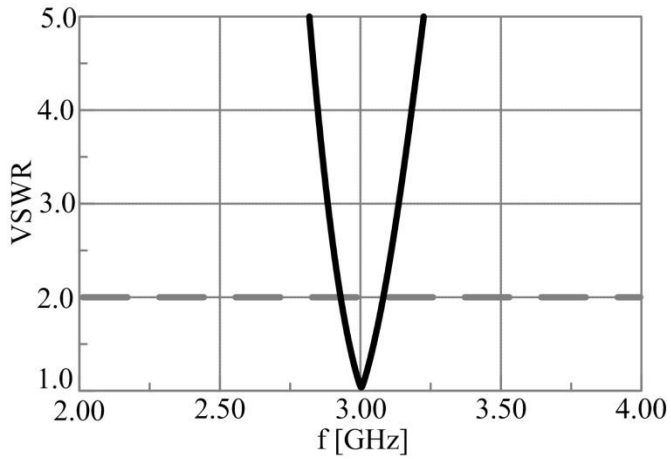

Fig. 11. VSWR of an ideal resonant patch antenna.

Fig. 12 (right) shows impedance vs. frequency. Note the resistance and reactive curves vary with frequency. The imaginary impedance component determines the resonant frequency based on where the imaginary line crosses zero. Fig. 12 (left) shows S_{11} plotted on a Smith chart. The Smith chart provides a graphical representation of all real and complex number combinations from $-\infty$ to $+\infty$ as a function of frequency. Dividing the chart into two hemispheres, the top half represents positive complex numbers (inductive), and the bottom half contains negative complex numbers (capacitive). The center represents a perfect match and the dashed circle illustrates the 2:1 VSWR bandwidth.

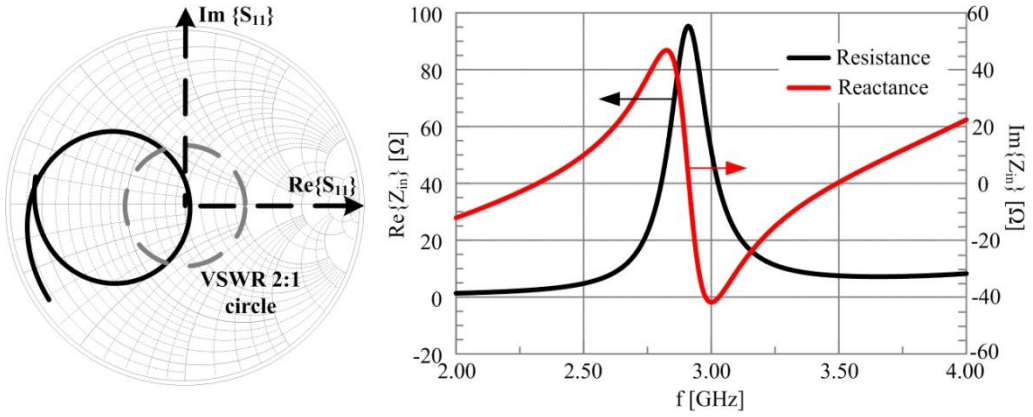

Fig. 12. Smith chart plot of S_{11} (left) and rectangular impedance plot (right).

CHAPTER IV

THE COAXIAL STUB MICROFLUIDIC IMPEDANCE TRANSFORMER (COSMIX)

A. Physical Model

The coaxial stub microfluidic impedance transformer (COSMIX) originated from the idea of measuring the permittivity and permeability of colloidal dispersions. Connecting the COSMIX with microfluidic capillaries allowed operation as a dynamic impedance transformer. Other adaptive matching devices have been developed [2, 18-19, 47] using RF MEMS as stubs and RLC lumped circuit components. Removing the matching network and voltage bias wires needed for RF MEMS chips, the COSMIX has the geometry of a small hollowed coaxial transmission line segment L = 10 mm. A SMA probe terminates the COSMIX on one end and a small gap d = 0.22 mm terminates the other. The closed nature of the coax and a small gap-termination are suitable for fluid-flow.

B. Analytical Model

EFCDs vary the transmission line properties of distributed structures and equivalent circuit parameters of lumped elements. Both are key elements in the microfluidic impedance transformer design. Fig. 13 shows a lossy transmission line of length dl, with complex propagation constant γ, complex characteristic impedance Z_0, and loaded with a nominal complex termination Z_T.

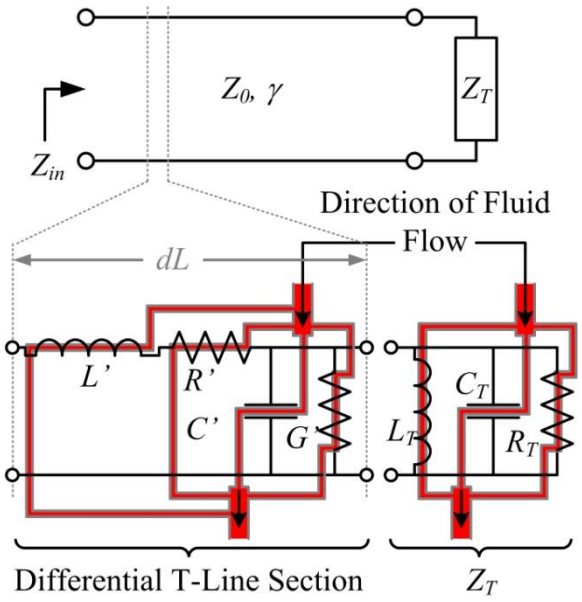

Fig. 13. Illustration of EFCDs applied to both transmission lines and circuits.

Fig. 13 shows the equivalent circuit (telegrapher) representation for a transmission line differential length *dl* with per unit length parameters R', L', G', and C' and a parallel RLC-circuit with R_T, C_T, and L_T replacing Z_T. EFCDs are flowing through these elements to illustrate the impact of changing ϑ in (1). Determining Z_0 and γ requires the transverse cross-section of the physical transmission line and the geometry of the load termination to find Z_T. In this basic configuration, changing ϑ within the termination and/or transmission line facilitates the ability to dynamically transform the load impedance seen at the input to this line (Z_{in}) – all parameters R', L', G', C', R_T, C_T, and L_T, are a function of ϑ and the EFCD constitutive parameters. In Fig. 13, there are five equations (17-21) representing the components.

$$L'(\vartheta) = \frac{\mu(\vartheta)}{2\pi} \ln \frac{b}{a} \tag{17}$$

$$C'(\vartheta) = 2\pi\varepsilon'(\vartheta) \Big/ \ln\frac{b}{a} \tag{18}$$

$$R_s'(\vartheta) = \sqrt{\frac{\omega\mu(\vartheta)}{2\sigma(\vartheta)}} \tag{19}$$

$$R'(\vartheta) = \frac{R_s'(\vartheta)}{2\pi}\left(\frac{1}{a}+\frac{1}{b}\right) \tag{20}$$

$$G'(\vartheta) = 2\pi\omega\varepsilon''(\vartheta) \Big/ \ln\frac{b}{a} \tag{21}$$

Inductance (17) comes from the self-inductance of the two conductors. Shunt capacitance (18) results from conductor coupling. Resistance (19-20) originates from the metal surface resistance in the conductors and (21) finite conductivity of the conductors. Each equation relates back to the inner conductor radius *b*, outer radius *a*, and material parameters (ε, μ, σ). The conductivity (σ) comes from the metal of the conductor, usually copper or gold. The material parameters (ε, μ) are complex (22-23) with tan(δ_e) as the dielectric loss tangent and tan(δ_m) called magnetic loss tangent.

$$\varepsilon = \varepsilon_0\varepsilon_r\left(1 - j\tan(\delta_e)\right) \text{ or } \varepsilon = \varepsilon' - j\varepsilon'' \tag{22}$$

$$\mu = \mu_0\mu_r\left(1 - j\tan(\delta_m)\right) \text{ or } \mu = \mu' - j\mu'' \tag{23}$$

Each transmission line has characteristic impedance based on the dielectric, conductor radii, and operating frequency. Because of the line's lossy nature, *R'*, *L'*, *G'*, and *C'* are used to determine the characteristic line impedance (24)

$$Z_0' = \sqrt{\frac{R' + j\omega L'}{G' + j\omega C'}} \tag{24}$$

If the load attached to the transmission line, does not match the characteristic impedance of the line, reflections occur and a standing wave results. The reflection coefficient, Γ determines the ratio of reflected waves to incident waves (28) at the load. Determining the reflection coefficient at the opposite end of the line requires adding a phase term. This phase term takes into consideration the round trip of the wave (i.e. generator to load and back to generator), change in propagation constant, length of the line, and attenuation (29). The transmission line input impedance changes with the lossy load attached, and finding the new input impedance (30) in conjunction with the reflection coefficient, determines the tuning circuit required to match the load to the line.

$$\Gamma = \frac{Z_T - Z_0^{'}}{Z_T + Z_0^{'}} \tag{25}$$

$$\Gamma(l) = \Gamma e^{-2j\beta l} e^{-2l\alpha} = \Gamma e^{-2\gamma l} \tag{26}$$

$$Z_{in} = Z_0^{'} \frac{Z_T + Z_0^{'} \tanh(\gamma l)}{Z_0^{'} + Z_T \tanh(\gamma l)} \tag{27}$$

The wave number or propagation constant β, relates to the number of radians per unit length. When losses are present in the transmission line, wave attenuation α (Nepers per unit length) needs to be included. Both β and α are extracted from the propagation constant γ (24-26).

$$\gamma = \sqrt{(R + j\omega L)(G + j\omega C)} \tag{28}$$

$$\beta = \omega\sqrt{LC} \tag{29}$$

$$\alpha = \frac{1}{2}\left(R\sqrt{\frac{C}{L}} + G\sqrt{\frac{L}{C}} \right) \tag{30}$$

Variable EFCD ϑ transforms the load impedance to the transmission line impedance acting as matching stubs. Matching stubs are modeled as reactive elements (i.e. capacitors and inductors) attached to a transmission line for tuning the reactive line impedance with a load. They are shunt and series elements designed for operation with a specific application, load, and frequency [48]. The COSMIX *'s* gap termination provides the reactive impedance.

Fig. 14 illustrates a transmission line terminated with an air gap then a short. N. Marcuvitz developed an equivalent circuit model as a capacitor (31) [49]. This equivalent circuit remains valid only if (32) [49] is satisfied. The gap distance (*d*) has to be within the bounds of (33) [49]. When the gap distance *d* has grown outside the bounds, additional capacitance needs to be included in the circuit model. If *d* is much greater than (33), then the coax has coupled into a circular waveguide.

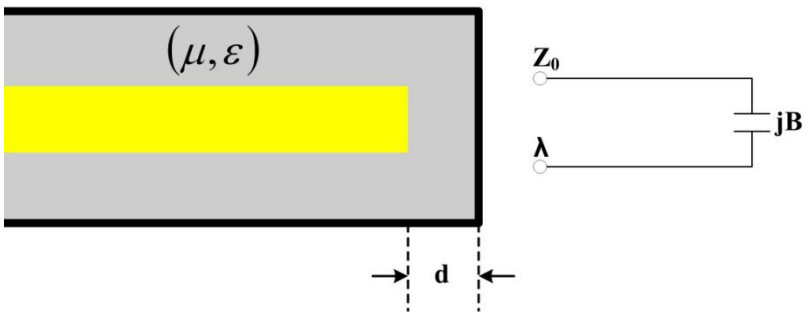

Fig. 14. A coaxial transmission line with a gap-termination and an equivalent circuit.

$$\frac{B}{Y_0} = \left(\frac{4b}{\lambda_0}\ln\frac{a}{b}\right)\left(\frac{\pi}{4}\frac{b}{d} + \ln\frac{a-b}{d}\right) \tag{31}$$

$$\lambda > 2(a-b)/\gamma_1 \text{ where } \pi\gamma_1 = \left(\frac{a}{b} - 1\right)3.142 \tag{32}$$

$$2\pi d/\lambda << 1 \text{ and } d/(a-b) << 1 \tag{33}$$

When the capillaries are attached to a transverse electromagnetic (TEM) coaxial structure, they function as a dielectric circular waveguide. Fig. 15 shows the basic circular waveguide geometry with radius *a*. When a TEM propagating wave in the coax intersects the capillary, a transverse magnetic (TM) wave may be excited and begin propagating in the capillary. Fig. 16 shows how TEM to TM wave may result.

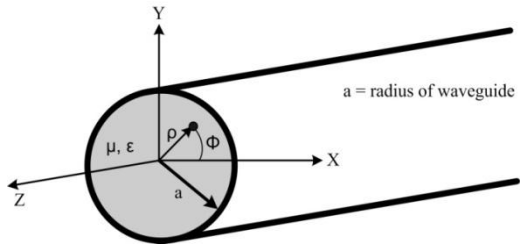

Fig. 15. Illustration of a circular waveguide geometry representing a microfluidic capillary.

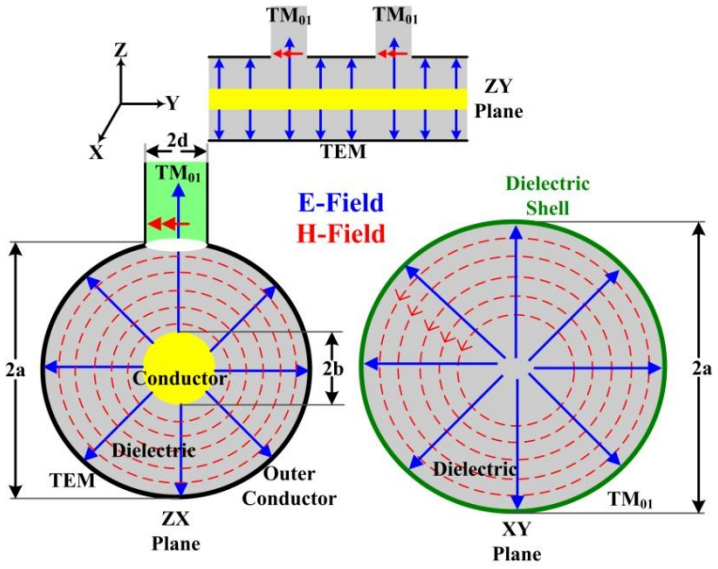

Fig. 16. Shows as a TEM wave propagating across the capillary entrance exciting a TM wave.

As the TEM wave passes by the capillary opening, part of the electric field couples into the capillary. The *z* traveling electric field has a transverse magnetic component forming a TM mode. The circular waveguide impedance depends on the radius, material properties (ε, μ), and cutoff frequency (34) [50] with x_{mn} referring to the Bessel function zero. A TM waveguide, operating below the cutoff frequency, causes the characteristic impedance (35) to be imaginary and capacitive. Therefore, the capillary equivalent circuit is a shunt capacitor.

$$f_{cmn}(\vartheta) = x_{mn} \Big/ \left(2\pi a \sqrt{\mu(\vartheta)\varepsilon(\vartheta)}\right) \tag{34}$$

$$Z_{mn}^{TM_z}(\vartheta) = -j\sqrt{\mu(\vartheta)/\varepsilon(\vartheta)}\sqrt{\left(f_c(\vartheta)/f\right)^2 - 1} \tag{35}$$

Fig. 17 shows the cutoff frequency for three different circular waveguide radii as a function of permittivity. With the capillary radius forcing cutoff, the circular

waveguide attenuates and propagation ceases, causing negligible power loss. No wavelength definition exists below cutoff caused by the exponentially wave decay.

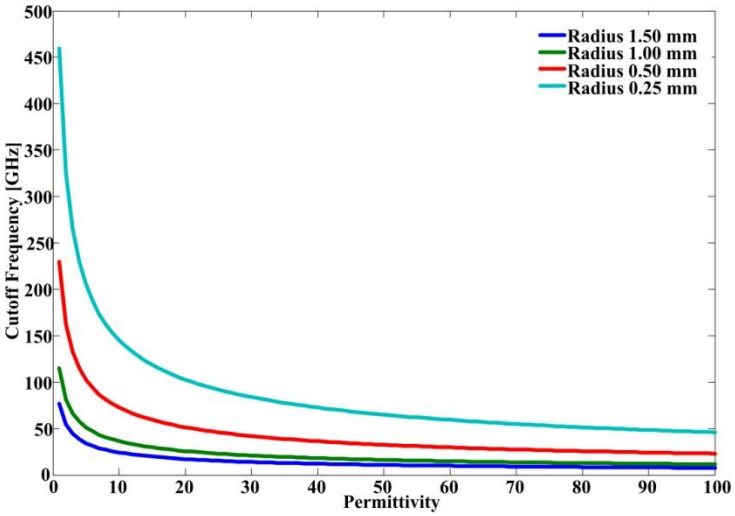

Fig. 17. Illustration of TM cutoff frequency for three different radii.

Fig. 18 shows a cross-section of the COSMIX and its equivalent circuit. The COSMIX circuit has three main components: gap-termination, microfluidic inlet and outlet, and the coax line. All components are a function of ϑ. Physically, the COSMIX has a small length L = 10 mm of hollow coaxial transmission line (outer and inner radii a = 2.05 mm and b = 0.615 mm, respectively) terminated in a shielded (capped) open-circuit with a gap size d = 0.22 mm. The gap-termination was represented by a variable capacitor using (36) (modified from (31) [49]) and R_T to include EFCD losses. The microfluidic inlet and outlet was equivalent to a capacitor using (35). Coax impedance (24), a function of ϑ, included any EFCDs losses. The COSMIX model was coded in Matlab using (17-36) to perform the calculations and is available in the Appendix.

Analytical results provided a reactive loop (capacitive to inductive tuning) around the Smith chart.

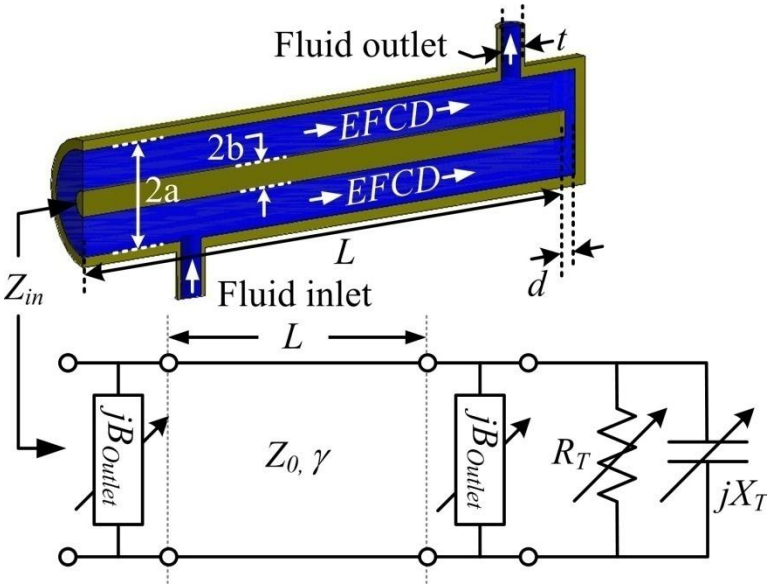

Fig. 18. Cross-section of simulated model (HFSS) and equivalent circuit model used to study the trends and performance of the COSMIX with EFCDs.

$$X_T^{Cap}(\vartheta) = Z_0(\vartheta)\left(4af\sqrt{\varepsilon_{eff}(\vartheta)\,\mu_{eff}(\vartheta)}\ln\frac{b}{a}\right)\left(\frac{\pi}{4}\frac{a}{d}+\ln\frac{b-a}{d}\right) \tag{36}$$

C. CAD Model

Two HFSS COSMIX models were designed to verify the analytical results and assist in fine-tuning. The first model did not contain the microfluidic channels in Fig. 18. The second model did contain the channels. Both the CAD (HFSS [51]) and analytical models include the fluid inlet and outlet (both of diameter *t*) at the structure's linear edges, creating the potential for fluid flow down the line length and within the gap-

termination. The CAD model channels were treated analytically as circular waveguides connected in parallel to the coaxial line. Without careful attention, the electric field within the coaxial line will excite a TM mode in these channels. Thus, the dimension *t* and EFCD effective material properties are chosen such that COSMIX operation remains well below cut-off for any guided modes in the channels. The waveguide reactive characteristic impedance in cut-off represents them. Fig. 19 (left) shows an admittance Smith chart with a shunt reactive element or capacitor. As the frequency increases, the admittance decreases, and the capacitance acts like an open circuit. Fig. 19 (right) shows the TM waveguide impedance in cutoff. The waveguide has a 22 GHz cutoff frequency, well beyond the COSMIX's current operating region of 400 MHz to 3 GHz. As frequency increases, and permittivity increases, impedance decreases. By inversing the impedance, the admittance increases in terms of increasing frequency and decreasing as permittivity increases. Therefore, the TM waveguide is as an open circuit.

After extensive parameter sweeps, it was determined that the loading effects from these structures were negligible (similar to having very large capacitors in parallel with the line). To show there was no difference between the models, two different ϑ {0% and 50%} were simulated. Fig. 20 shows the COSMIX with and without capillaries. Analytical and simulations have confirmed that the microfluidic channels (when properly designed) act as large shunt capacitors along the line and contribute nominal additional circuit loss-mechanisms.

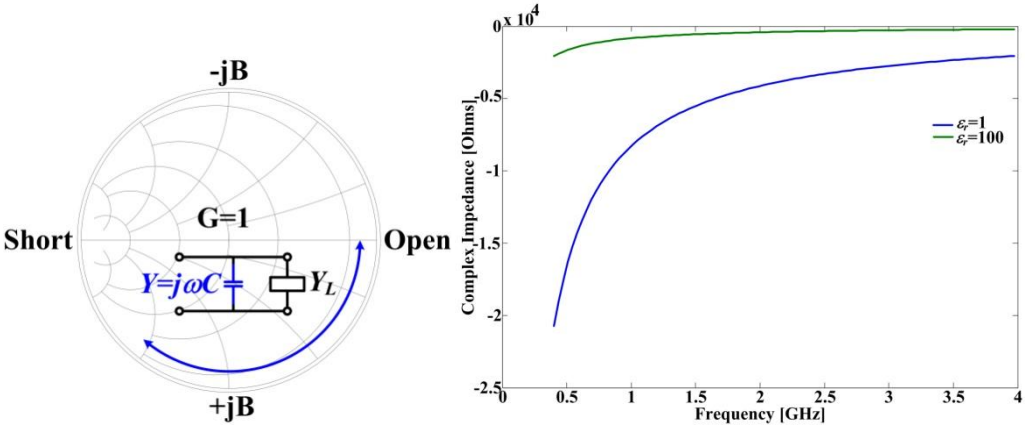

Fig. 19. Admittance Smith chart showing shunt reactance (left) and impedance of a TM waveguide in cutoff (right).

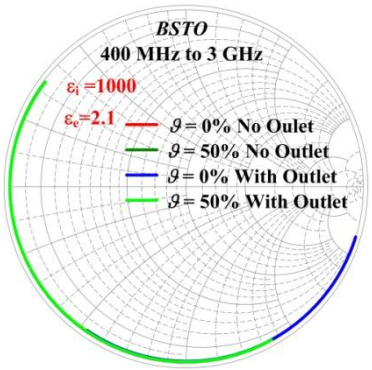

Fig. 20. Simulation results for the COSMIX with and without micofluidic capillaries.

D. Fabricated Device

The COSMIX was fabricated using a piece of aluminum stock. Fig. 21 shows the COSMIX fabrication design and dimensions. Initial design fabrication limitations prevented channel construction. Channel electromagnetic contribution remains negligible and this structure accurately evaluates the performance during static (non-flowing) conditions. However, as size decreases to nano-scale dimensions their

contribution is expected to increase. Further research is anticipated. This mixing and flowing within the device creates gradients of EFCD properties that result in tapered impedance and propagation characteristics, which are currently under investigation.

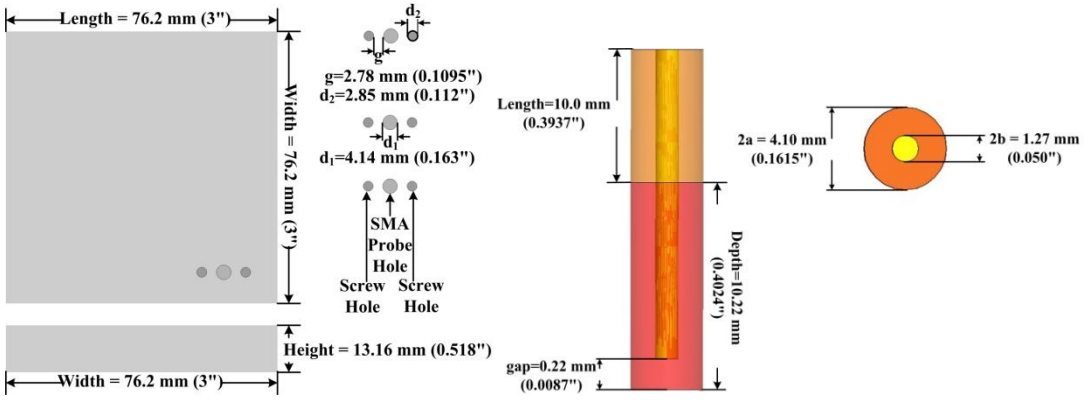

Fig. 21. The COSMIX design parameters for initial fabrication.

E. Results

Colloidal Barium Strontium Titanate (BSTO) [43] (ε_{r2} ~ 1000 and tan(δ_2) ~ 0.01) was treated with Nanosperse™ surfactant [45] (ε_r ~ 8 and tan(δ) ~ 0.11), and then dispersed into low-loss petroleum distillate (ε_{r1} ~ 2.1 and tan(δ_1) ~ 0) at two different ϑ {0% and 50%} to achieve EFCDs with ε_{eff} {2.1 and 8} and tan(δ_2) {0 and 0.03}, respectively. Fig 22 shows the fabricated structure, beakers of the EFCDs and the measured, modeled, and simulated results at 400 MHz, 800 MHz, and 1.6 GHz, respectively, for ϑ {0% and 50%}.

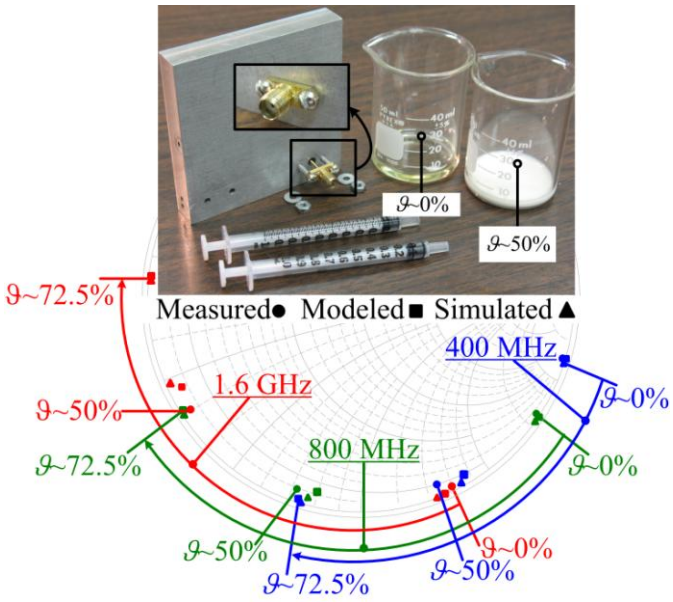

Fig. 22. Fabricated COSMIX and EFCDs used in experiments.

The Smith chart was chosen for its ability to demonstrate the reflect-line phase shifting ability of the COSMIX [11-12] as well as the effects from losses. This plot illustrates the significant tunability achieved from fluidic devices using dynamic material systems. Modeled and analytical results provide a full loop around the Smith chart (tuning from inductive to capacitive). Measured results for higher ϑ were not available, but Fig. 22 demonstrates the excellent agreement between theory, simulation, and measurement.

CHAPTER V

A FREQUENCY RECONFIGURABLE PATCH ANTENNA

A. Physical Model

Transitioning from circuits to antennas, a microstrip patch antenna was designed to test EFCD frequency reconfiguration properties. The linearly polarized patch antenna shown in Fig. 8 has a rectangular geometry (W = 50 mm and L = 43.5 mm). The Rochelle foam substrate has height h = 4 mm. Three microfluidic capillaries, each with a 3 mm diameter, were imbedded in the substrate.

B. Analytical Model

The analytical model originates from material perturbation of the rectangular patch antenna cavity model. Material perturbation occurs from a cylindrical capillary of diameter d (containing EFCDs), which changes the cavity's resonant frequency (37) [52]. Component vectors $\boldsymbol{E_0}$ and $\boldsymbol{H_0}$ represent the initial electric and magnetic fields in the cavity, while $\boldsymbol{E}$ and $\boldsymbol{H}$ represent the electric and magnetic field vectors after a small material ($\Delta\varepsilon$, $\Delta\mu$) perturbation.

$$\frac{f - f_0}{f_0} \approx -\iiint_{Cavity} \left(\Delta\varepsilon\vec{E}\bullet\vec{E}_0^* + \Delta\mu\vec{H}\bullet\vec{H}_0^*\right)d\tau \Big/ \iiint_{Cavity} \left(\varepsilon\vec{E}\bullet\vec{E}_0^* + \mu\vec{H}\bullet\vec{H}_0^*\right)d\tau \qquad (37)$$

For small perturbations (i.e., $\Delta\varepsilon$ or $\Delta\mu$ approach zero) in the resonant cavity, the resonant frequency decreases slightly. A succession of incremental changes provides a large change in ε or μ, thus causing a large frequency decrease. It is important to note

that a small change in ε where the E-field nears zero, or likewise μ where the H-field nears zero does not decrease the resonant frequency. Thus, the placement and orientation of the capillary that will garner maximum effect depends on the EFCD constitutive parameters (ε, μ). Fig. 23 shows the fluidic capillaries imbedded in the antenna substrate and their proper position based on EFCD material. The dielectric capillaries are located along the radiating edges (where the electric field is a maximum). The magnetic capillaries are located at the patch center (where the magnetic field is a maximum). This thesis considers both dielectric and magnetic EFCDs oriented across the patch width.

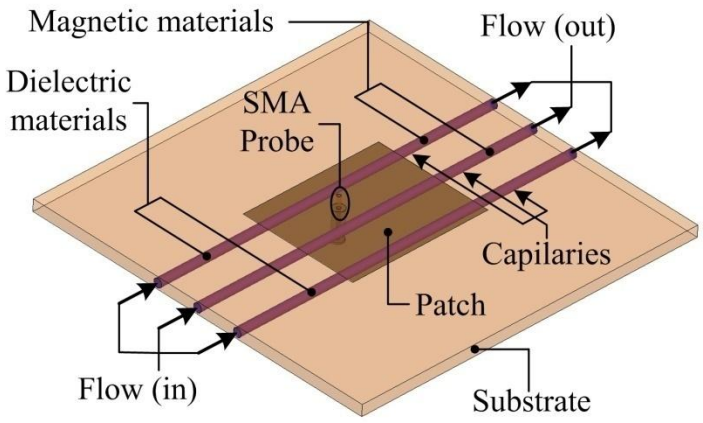

Fig.23. Microstrip patch antenna with distinguished capillaries.

The reconfigurable antenna design then examined the patch transmission line model outlined in Chapter III, with special consideration given to the electrical length about the feed location in the length direction. The ratio of these two electrical lengths should remain constant throughout the range of reconfigured states (e.g., from having a minimum to maximum ϑ of colloidal materials dispersed in the EFCD) to maintain an

appreciable 2:1 VSWR impedance bandwidth. This infers first and third capillary placements along the radiating edges and second capillary placement at the center; thus, proper capillary placement alters the electrical length extensions on both sides of the probe.

The reconfigurable antenna has a fixed physical length and a reconfigurable electrical length that decreases as the material properties increase. Provided the impedance match does not change significantly as the effective material properties of the EFCD increases, the gain of the structure will decrease and the beam width will increase accordingly. Maximum gain occurs when the EFCD material properties are lowest. Avoiding capillary placement at the patch edges preserves antenna radiation behavior.

C. Fabrication

Fig. 24 shows the fabricated antenna. This design uses Rochelle foam substrate (ε_r = 1, μ_r =1, and σ_r = 0 S/m) of height h = 4 mm and patch length L = 43.5 mm and width W = 50 mm. Copper sheeting was used to create the patch. Three thin-walled plastic coffee straws (d = 3 mm) served as capillaries. The straw permittivity closely matches the petroleum distillate oil permittivity.

Barium Strontium Titanate (BSTO) [43] (ε_{r2} ~ 1000 and tan(δ_2) ~ 0.01) was treated with Nanosperse™ [45] surfactant (ε_r ~ 8 and tan(δ) ~ 0.11), and then dispersed into low-loss petroleum distillate (ε_{r1} ~ 2.1 and tan(δ_l) ~ 0) at two different ϑ {0% and 50%} to achieve EFCDs with ε_{eff} ~ {2.1 and 8.3} and tan(δ_{eff}) ~ {0 and 0.02},

respectively. Since the surfactant ϑ was small (< 2.5%), this material was not included in the calculations of effective material properties.

Strontium hexaferrite ($\varepsilon_{r2} \sim 5$, $\mu_{r2} \sim 2$, and $\sigma_{r2} \sim 0.03$) (from [53-54]) powder was similarly dispersed into a low-loss petroleum distillate ($\varepsilon_{r1} \sim 2.1$ and $\tan(\delta_l) \sim 0$) at two different ϑ {0% and 50%} to achieve EFCD characteristics from the Maxwell Garnett mixing rule with $\varepsilon_{eff} \sim$ {2.1 and 3.3}, $\mu_{eff} \sim$ {1 and 1.4}, and $\tan(\delta_{eff}) \sim$ {0 and 0}, respectively.

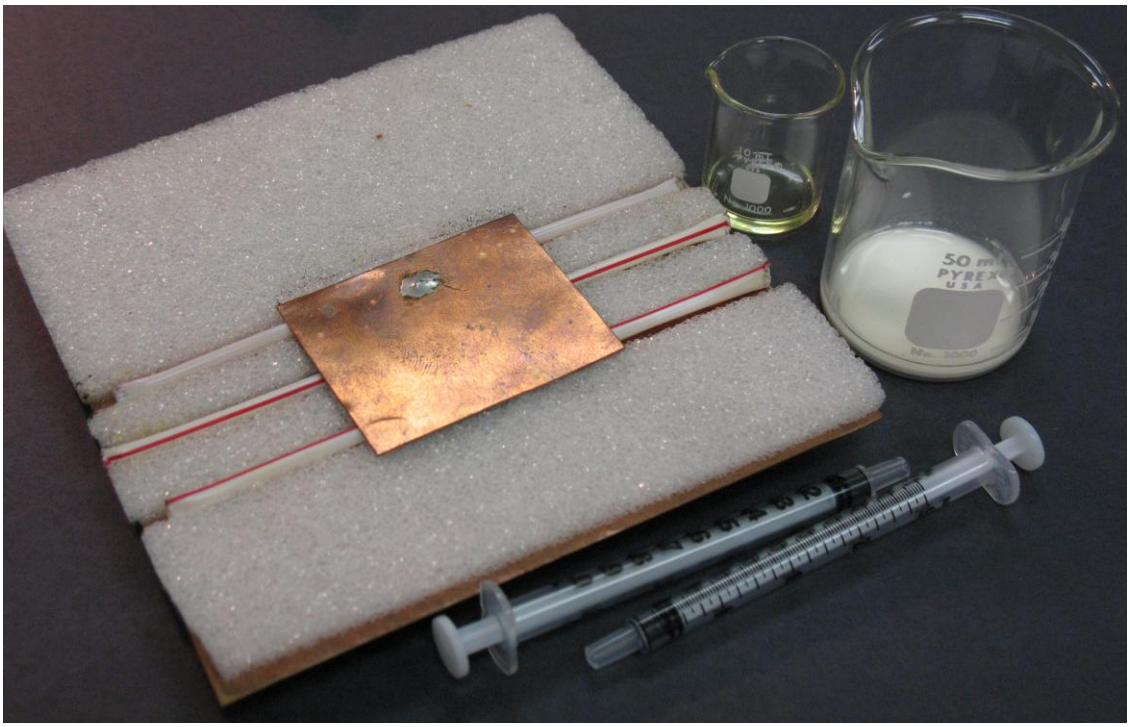

Fig. 24. Fabricated model of the microstrip patch antenna with capillaries embedded in the substrate material.

D. Results

Fig. 25 shows the VSWR response and input impedance for the ϑ {0%, 25%, 50%, and 92.5%}. A ϑ = 0% represents 100% oil and ϑ = 50% a 50:50 mixture of oil and colloidal material. The ϑ = 25% in the capillaries reconfigured the resonant frequency from 3 GHz to 2.9025 GHz (for a total frequency shift of 97.5 MHz). A ϑ = 50% reconfigured the resonant frequency 3 GHz to 2.85 GHz (for a total frequency shift of 150 MHz). The ϑ = 92.5% reconfigured the resonant frequency from 3 GHz to 2.7 GHz (for a total frequency shift of 300 MHz). De-ionized water emulated the upper ϑ limit of BSTO. The Smith response demonstrates little impedance locus change for all three states.

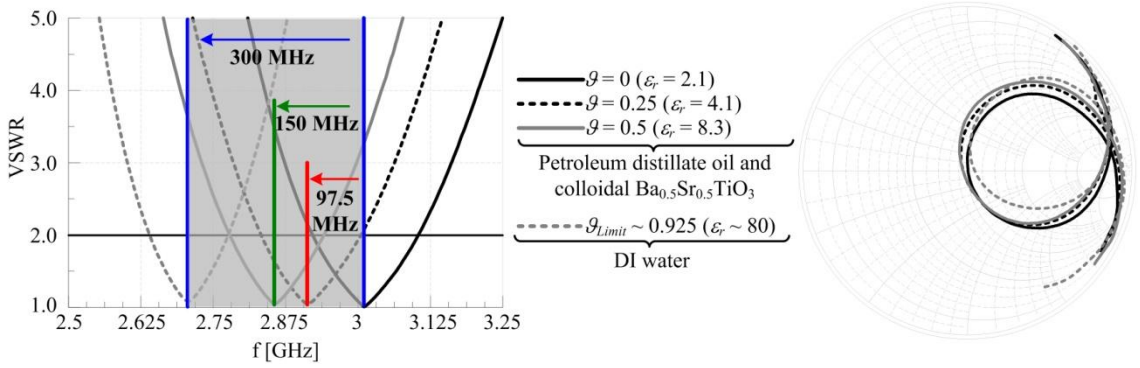

Fig. 25. Measured VSWR (left) and input impedance (right) as a function of BSTO ϑ.

Fig. 26 shows that the strontium hexaferrite experiment obtained the expected VSWR trends. The addition of strontium hexaferrite material in the capillaries reconfigured the resonant frequency from 3.006 GHz to 2.965 GHz (for a total shift of

41 MHz). The Smith chart demonstrates very little impedance locus change for both states.

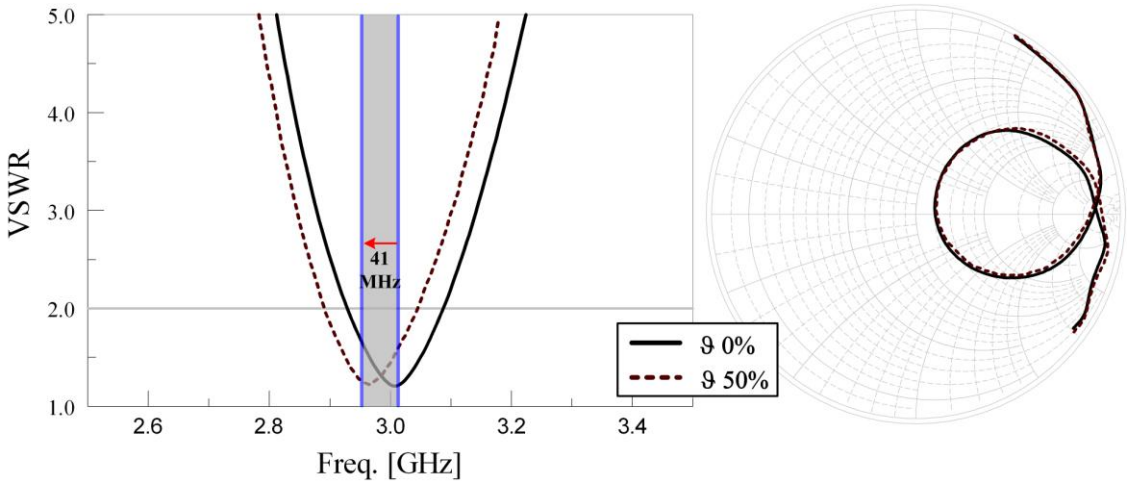

Fig. 26. Measured VSWR (left) and input impedance (right) as a function of strontium hexaferrite ϑ.

Figs. 27 and 28 show measured patterns for the ϑ = 0% and ϑ = 50% respectively. Fig. 27 shows no radiation pattern abnormalities in both ϑ = 0% experiments and provides a basis for comparison when the ϑ increases. Fig 28 shows a net decrease in gain, about 2 dB, occurs as the BSTO ϑ increases. Fig. 28 shows a negligible pattern change compared with the BSTO because the small effective permittivity increase from the strontium hexaferrite did not impact the gain like the BSTO. The gain decrease occurred because of the decreasing aperture size as wavelength increases. Little differs between the two patterns, but they have been included to demonstrate the pattern stability through reconfiguration. Both patterns were normalized at the resonant frequency depending on its reconfigured state (where the

reconfigured absolute gain was normalized to the absolute gain of the initial frequency configuration).

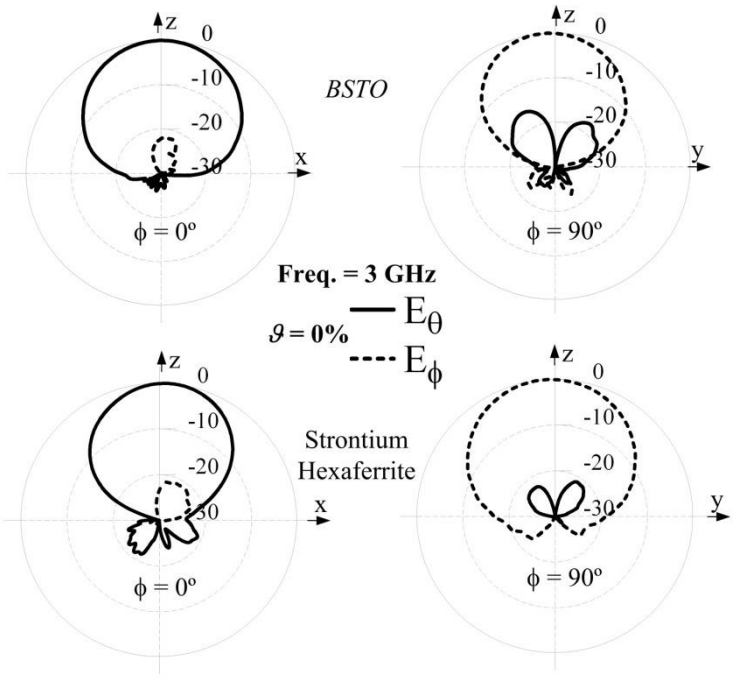

Fig. 27. Measured radiation patterns for the fabricated using a $\vartheta = 0\%$ (100% oil) in the capillaries BSTO (top) and strontium hexaferrite (bottom).

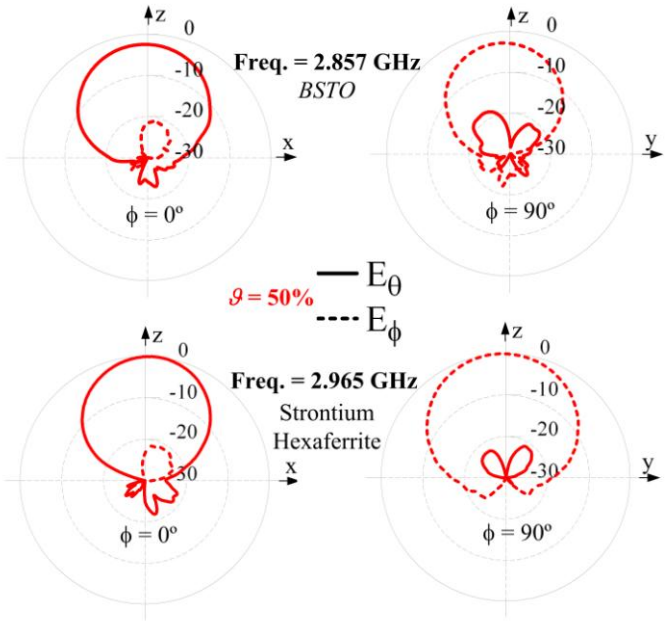

Fig. 28. Measured radiation patterns for the fabricated antenna using a $\vartheta = 50\%$ (50% oil and 50% colloidal material) in the capillaries BSTO (top) and strontium hexaferrite (bottom).

CHAPTER VI

A FREQUENCY RECONFIGURABLE PATCH ANTENNA ARRAY

A. Physical Model

Prior studies have shown the feasibility of integrating different pressure-driven reconfiguration mechanisms into the substrate of single element microstrip patch antenna to achieve frequency stability and reconfiguration [11 -17]. A small array experiment was conducted to include the ability to locally and globally reconfigure a multiple antenna system. The modeled array was a 1x2 linear array. The array designed and fabricated was fed using SMA probes.

B. E-Plane and H-Plane

Two different feed methods exist for microstrip antenna arrays -- series (H-plane) and corporate (E-plane). Mutual coupling between two-elements is partial to orientation (i.e., E-plane or H-plane) and separation distance between elements. E-plane (parallel) orientations are elements aligned collinearly along the antenna's E-plane. Likewise, H-plane (series) orientations are elements collinearly aligned along the H-plane.

C. CAD Model

The modular array design approach was used for the E- and H-plane case studies. The modular design method designs one patch antenna and then duplicates it to form an array. A silicone based elastomer called Sylgard 184 [24] or PDMS, was selected for the substrate because of its inert chemical composition, durability, and elasticity. The

estimated PDMS permittivity of 2.66 [55] was suitable for this testing platform. Limitations of the copper mold designed for the array required a substrate height of 5 mm. Three capillary channels with a diameter of 3 mm were embedded in the PDMS. The resonant frequency f_0 = 3 GHz.

The patch antenna, Fig. 8, was designed using the transmission line method described in Chapter III. The patch was calculated to have W = 28.79 mm and L = 36.96 mm. CAD simulation verified the results and tuned the coaxial probe position for a good impedance match. Simulation resulted in design parameters of W = 27.9 mm, L = 37 mm, and a = 5.7 mm. Fig. 29 shows the H-plane array layout. Half-wavelength element spacing was chosen. Edge-to-edge element spacing S_e = 15 mm for the H-plane and S_e = 22 mm for the E-plane. The capillaries were placed across the patch width with two at the edge and one capillary in the patch center. The center capillary was filled with low-loss petroleum distillate ($\varepsilon_{r1} \sim 2.1$ and $\tan(\delta_1) \sim 0$) and remained static during testing. This capillary was built into the model for future reconfiguration with magnetic material. The two outer capillaries were filled with BSTO [43] ($\varepsilon_{r2} \sim 1000$ and $\tan(\delta_2) \sim 0.01$).

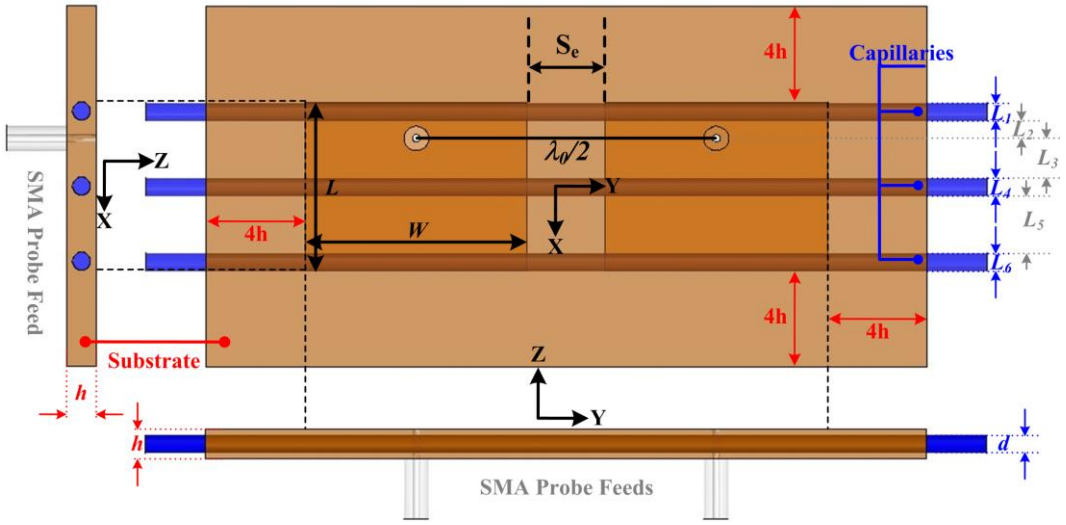

Fig. 29. CAD layout of the H-plane array.

Simulations were conducted on both orientations to examine the array behavior as the EFCDs progressed through the capillaries. The expression in (1) was programmed into HFSS [51] for varying ϑ of EFCDs. H-plane simulations were conducted in five steps and E-plane simulation in three. The simulated array data was de-embedded in HFSS.

The first element in the H-plane reconfigured before the second element, whereas the elements reconfigured simultaneously in the E-plane orientation. Fig. 30 shows the simulated results of the H-plane VSWR and Smith chart. Fig. 31 shows the simulated VSWR and Smith chart for the E-plane. Both antennas were matched at 3 GHz with a ϑ = 0%. The EFCDs in Fig. 30 and Fig. 31 are blue and the petroleum distillates are yellow. As the EFCDs progress through the array, special considerations are given to the electrical length about the probes. Fig. 10 shows the transmission line patch model. The ratio of effective lengths L_1 and L_2 should remain constant throughout the range of reconfigured states. If one effective length segment has become much longer than the other, then electrical position of the probe changes, affecting the impedance and detuning the antenna, seen in Figs. 30 and 31. In the final reconfigured state, both elements have shifted by 250 MHz, match the new 2.75 GHz resonant frequency, and have the same impedance.

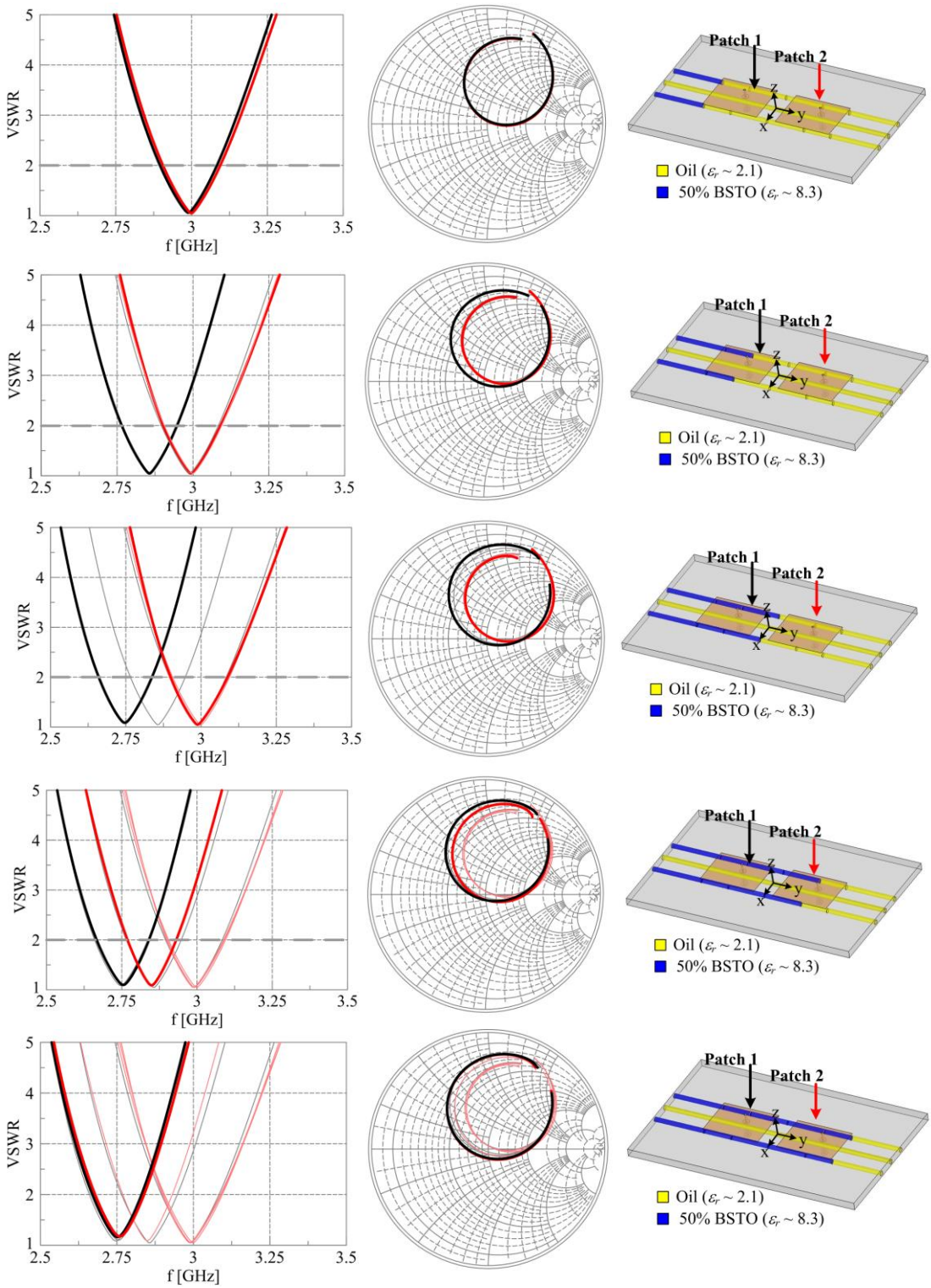

Fig. 30. H-plane simulation results showing the progressing EFCDs and changing VSWR and impedance data.

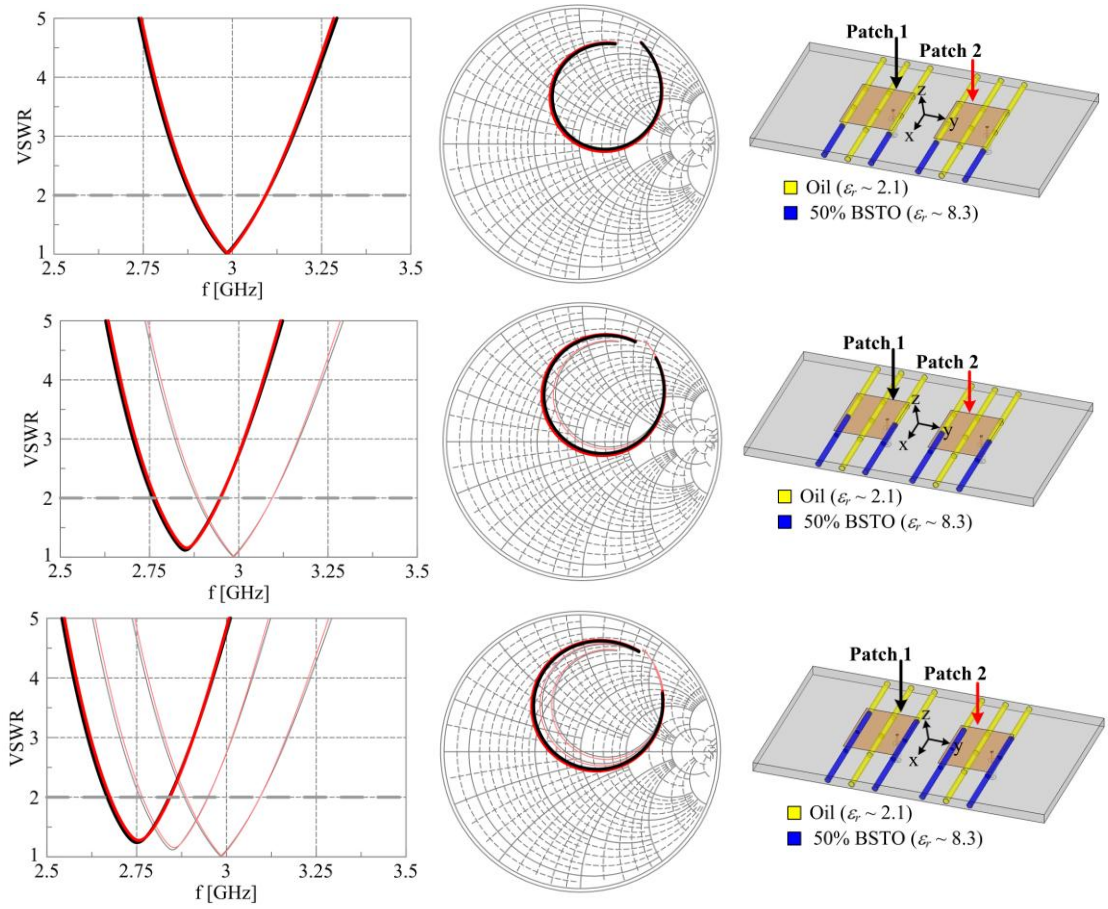

Fig. 31. E-plane simulation results showing the progressing EFCDs, changing VSWR, and impedance data.

Fig. 32 and Fig. 33 show the mutual coupling between elements for the H-plane and E-plane designs. As the EFCDs progress through, the edge-to-edge electrical length decreases and the permittivity increases, and the physical edge-to-edge separation S_e remains constant. The H-plane mutual coupling was higher than the E-plane because of the edge-to-edge spacing being less than the E-plane's spacing. Results showed a strong correlation between decreasing electrical length of the elements and an increase of the ϑ,

causing frequency to decrease and mutual coupling to increase. Increasing mutual coupling causes the array to detune.

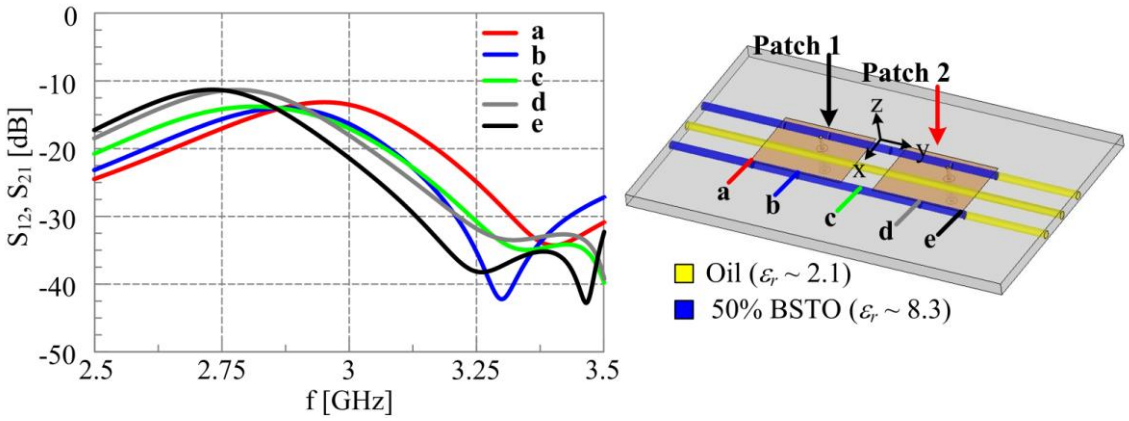

Fig. 32. Simulation of mutual coupling between elements of the H-plane array.

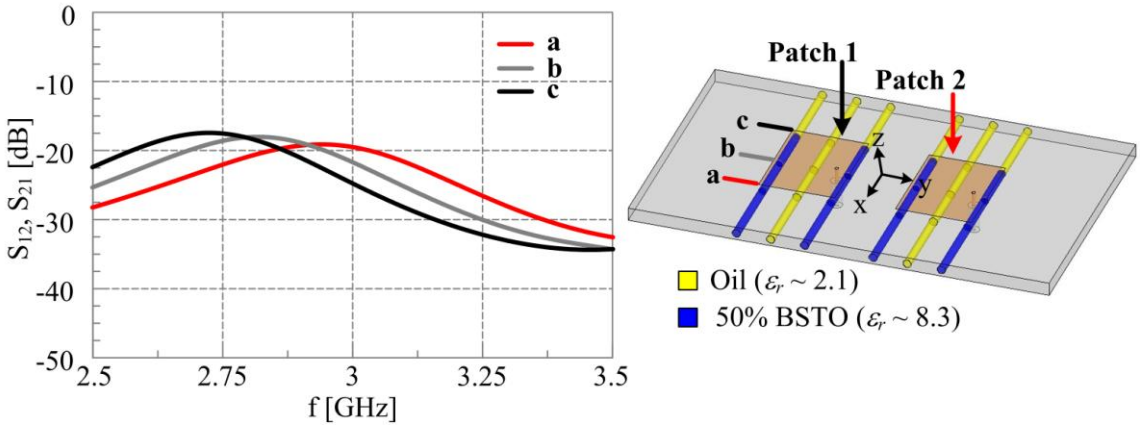

Fig. 33. Simulation of mutual coupling between elements of the E-plane array.

Fig. 34 shows a sample of the array patterns for the H-plane and E-plane designs after reconfiguration has completed. The multicolored array patterns represent the H-plane initial and final reconfiguration stages and all E-plane three reconfiguration

stages.The patterns have the same trends observed in the single element reconfiguration in Chapter V, but the addion of a second element adds a few additional effects including the array orientation. Unlike the radition patterns in Figs. 27 and 28, the array patterns are not normalized for clarity.

Surface waves are excited from the probe when the substrate permittivity is greater than one. The surface waves cause coupling between array elements. These waves reflect and diffract when they reach the edge of the substrate. The diffraction causes the end-fire or back lobe radiation seen in the H-plane and E-plane radiation patterns in Fig. 34. The back lobe level should remain less than -10 dB or the radiation efficeny of the antenna will be reduced [56]. Both H- and E-plane designs had a 0.6 dB drop in gain. Antenna gain decreases by from the losses in the EFCDs, increasing permittivity, and deceasing aperture size. The directivity decreases because of the decreasing electrical length between radiating apertures and array elements. Beamwidth widens because of the increasing effective patch length and decreasing resonant frequency. These results agree with the results in Figs. 27 and 28.

The H-plane design has some unique radiation features. Unlike the E-plane simultaneous element reconfiguration, the reconfiguring H-plane radiation patterns, not shown, have beamsteering resulting from the antennas reconfiguring consecutively. As the first element reconfigures to a lower resonant frequency, the aperture appears small because of the increasing wavelength. This causes the first element to appear larger. The second element remains at 3 GHz and original aperture size. Under these conditions, the first element acts as a reflector, the second element acts as a director, adjusting the beam

towards the smaller element, and forcing it off-axis as the EFCDs pass through. As the second element reconfigures, the beam begins to steer back to its original position.

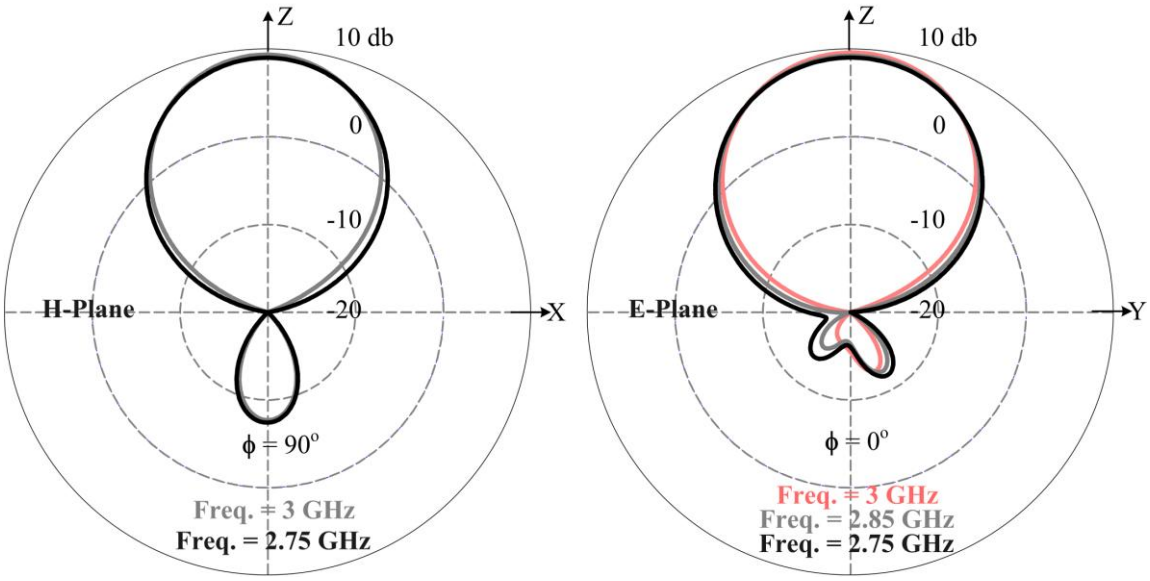

Fig. 34. Array radiation patterns for H-plane (left) and E-plane (right).

D. Fabrication

The fabrication of the 1x2 H-plane array began by making a copper mold for the PDMS substrate with three holes drilled on the sides to insert three 1/16 inch diameter stainless steel rods. The holes for the rod stood 1 mm from the ground of the mold. The length of the separation of the rods is seen in Fig. 35. 105.5 ml of PDMS basin and 10.6 ml of curing agent were mixed and poured onto the copper mold. The PDMS was baked for two hours in a chemical oven at 120°C. A copper ground plane was prepped and SMA probes soldered. Two pieces of copper tape formed the patch antennas. The elements were spaced half a wavelength apart. The substrate height was 5 mm.

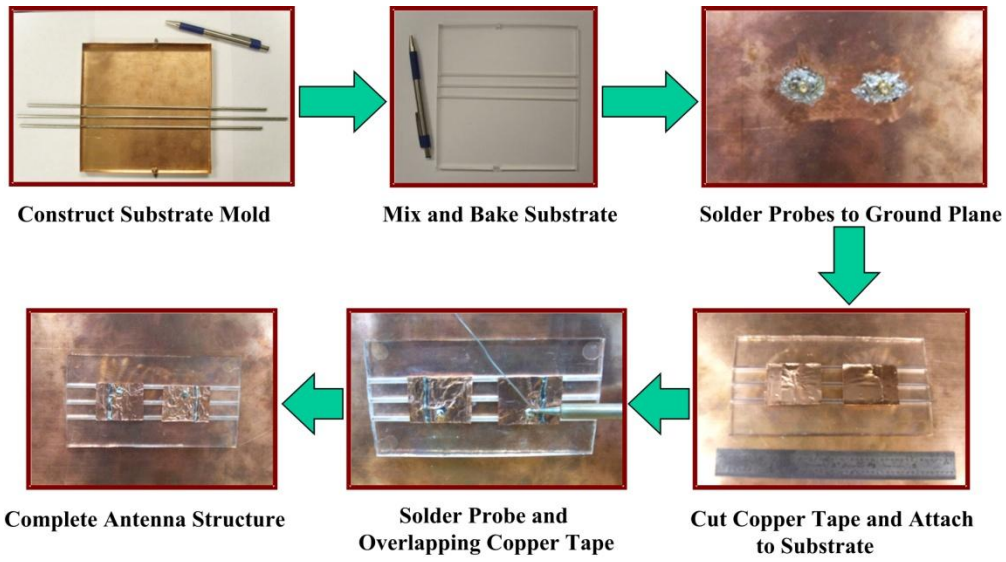

Fig. 35. Steps for fabrication of reconfigurable 1x2 patch antenna array.

E. Results

The EFCD mixtures contained BSTO (ε_{r2} ~ 1000 and tan(δ_2) ~ 0.01) and were dispersed in a low-loss petroleum distillate (ε_{r1} ~ 2.1 and tan(δ_1) ~ 0) at two different ϑ {0% and 50%}. Fig. 36 shows the test bench setup used during testing. Labview [57] controlled the syringe pump. A control valve switched between oil and EFCDs. The measurements were taken using an Agilent E8361C PNA network analyzer.

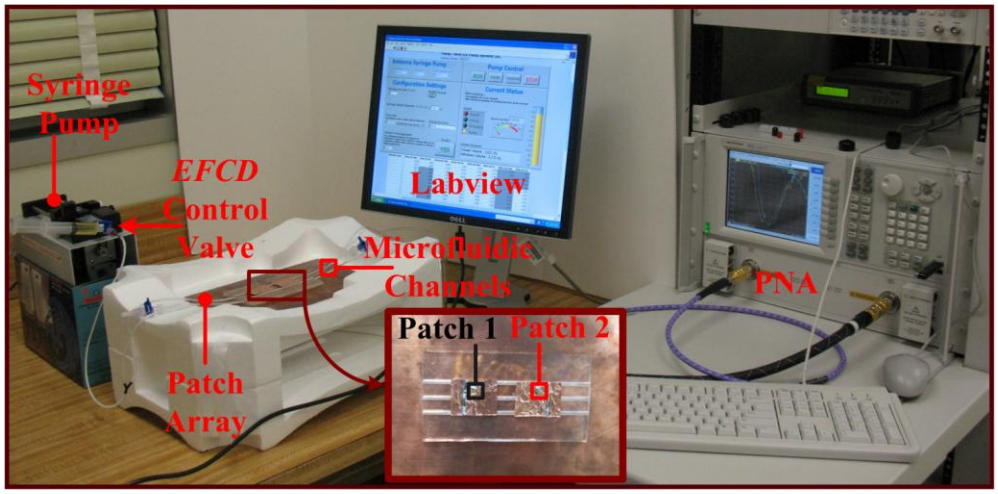

Fig. 36. Shows the reconfigurable array test bench setup and array result legend inset.

Fig. 37 shows the VSWR for the ϑ = 0% oil (top) and ϑ = 50% of BSTO (bottom). Elements one and two were closely matched at 3 GHz are with a VSWR of 1.5. The BSTO in Fig 37 (bottom) shifts the frequency, but the antennas are slightly detuned. Fig. 38 (right) shows a frequency shift of 170 MHz for the first element. Fig. 38 (right) shows a 140 MHz shift for the second element. The frequency shifts agree with the H-plane trends in Fig. 30 established during simulation.

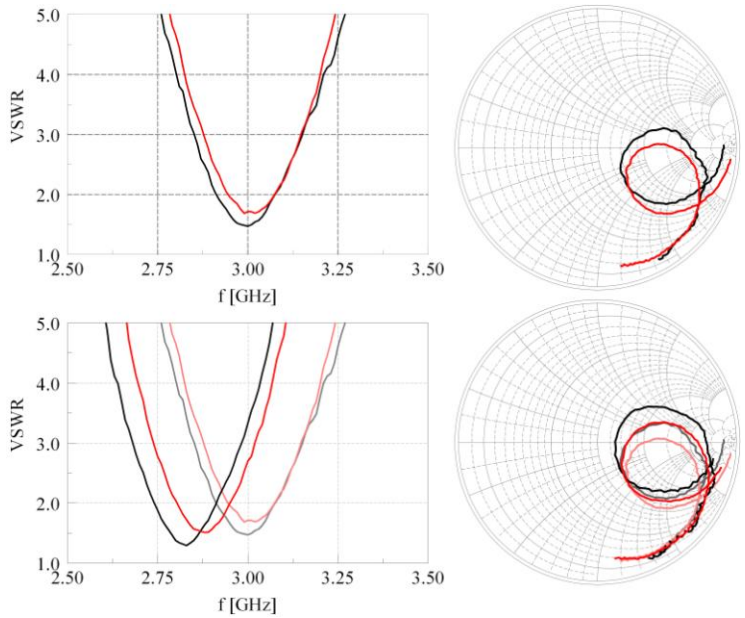

Fig.37. H-plane array with oil in all three capillaries (top) and array with BSTO in outer capillaries (bottom).

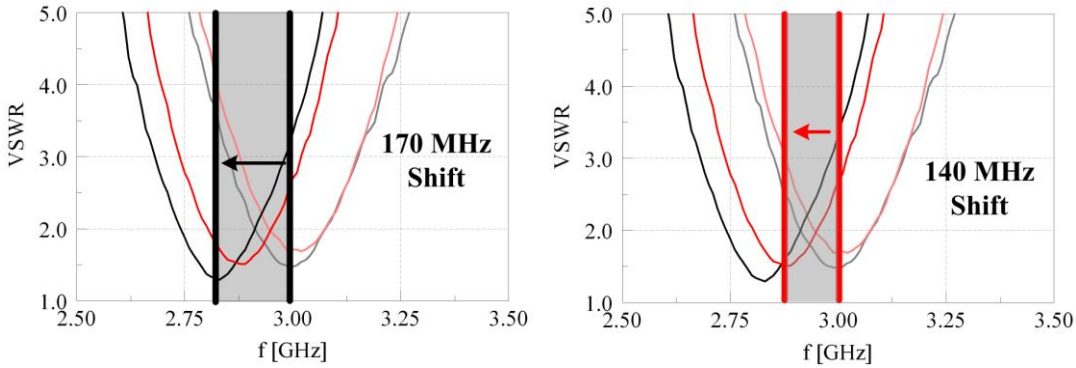

Fig. 38. Frequency shift of element one (left) and element two (right).

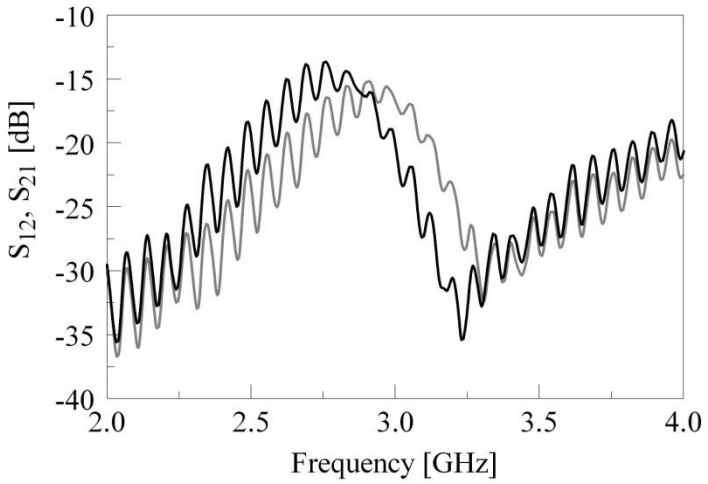

Fig. 39. Fabricated H-plane array mutual coupling with oil (grey) and $\vartheta = 50\%$ BSTO (black).

Fig. 38 (top) shows the mutual coupling of the array with only oil. Fig. 38 (bottom) shows the mutual coupling with the BSTO. The S_{21} signal has a ripple because of fabrication difficulties. The mutual coupling in Fig. 38 agrees with trends established in Fig. 32. As ϑ increases, the electrical length between the elements decreases, causing the coupling between antennas to increase. The fabricated H-plane array did agree with trends established by the simulations.

Several difficulties arose with fabrication of the H-plane array. The copper mold fabrication was constructed using hand tools instead of precision machinery. Error in the mold fabrication effected the capillary position and angle in the substrate. The capillaries were not located at the edge of the patch, unlike Fig. 29, but were partially positioned directly in the patch's fringing fields. This increased the radiating slot capacitances in the antennas, explaining the impedance difference between Figs. 30 and 36. The PDMS substrate naturally does not bond to adhesives. The antennas would rest on the PDMS

surface but would not remain at a fixed location. The non-stick PDMS nature caused the copper tape to roll at the corners causing the impedance to degrade and detune the antenna. Future designs will use a milled aluminum mold for the substrate and a milled thin copper clad Roger's Duriod sheet will replace the copper tape antennas.

CHAPTER VII

CONCLUSIONS

A pressure driven vascular network of functionalized colloidal dispersions has been presented for procuring a favorable trade-off in performance versus complexity over ‘wired’ SOA reconfiguration mechanisms and substantially increasing the electromagnetic agility in microwave circuits and antennas.

The COSMIX, patch antenna, and patch array have demonstrated the application of a vascular reconfiguration mechanism using Electromagnetically Functionalized Colloidal Dispersions (EFCDs). Analytical models were used to guide the placement of the capillaries, determine the reconfigurable properties, and examine material characteristics. A CAD model was simulated to examine the antennas and circuits (including losses) from the EFCDs.

The COSMIX results showed a full reactive loop (capacitive to inductive tuning) around the Smith chart over a 1.2 GHz bandwidth. A second microfluidic application demonstrated a novel antenna reconfiguration mechanism for a 3 GHz microstrip patch antenna. Results showed a 300 MHz downward frequency shift by dielectric colloidal dispersions and magnetic material produced a 40 MHz frequency shift. The final application demonstrated the dynamically altering microfluidic system for a 3 GHz 1x2 array of linearly polarized microstrip patch antennas. Both E- and H-plane designs showed a 250 MHz frequency shift by dielectric colloidal dispersions.

These results agreed well with trends predicted analytically. Measurements of the COSMIX, fabricated patch antenna, and patch array using dielectrically and magnetic based colloidal material. Microfluidic reconfiguration has opened the door for new types of adaptable RF applications using colloidal dispersions.

CHAPTER VIII

FUTURE WORK

Microfluidic reconfiguration has the potential to become a viable alternative to know SOA reconfiguration solutions. Several areas of further research could advance the technology. Such advancements include new dielectric and magnetic colloidal material having a poly-disperse nature allowing higher dispersion volume fractions and examining the impact of particle geometry and asymmetry. Further analysis and experimentation on high permittivity and permeability values are required for a more comprehensive understanding of their perturbation and affects in other RF applications. Enhance space based RF systems by researching colloidal dispersion response to gravitational and micro-gravitational interactions with microfluidic reconfiguration.

Designing the ability to recycle the colloidal particles or internally manipulating them will enhance the dynamic capabilities of microfluidic reconfiguration. Separation and removal of the EFCD sols involves the application of an electromagnetic field within the microfluidic structure. Placing the colloid in the presence of an electromagnetic field allows some control relating to Brownian motion or characteristic speed and direction of individual particles. These exerted forces align the particles for dispersion, separation, and removal. This provides the freedom to make the colloidal dispersion as dense or as sparse depending on the need at a specific moment in time.

REFERENCES

[1] B. Lakshminarayanan and T. Weller, “MEMS phase shifters using cascaded slow-wave structures for improved impedance matching and/or phase shift,” in *IEEE MTT-S Int. Microwave Symp. Dig.*, Jun. 6-11, 2004, pp. 725-728.

[2] M. Unlu, K. Topalli, H. I. Atasoy, E. U. Temocin, I. Istanbulluoglu, et al., "A reconfigurable RF MEMS triple stub impedance matching network," in *Proc. of 36th Microwave Conference*, Manchester, UK, Sept. 10-15, 2006, pp. 1370-1373.

[3] K. Brito and R. N. de Lima, "Tunable impedance matching network," in *Proc. of Microwave and Optoelectronics Conference,* Oct. 29-Nov.1, 2007, pp. 117-121.

[4] M. Popov and S. He, "Design of an automatic impedance-matching device," *Microwave and Optical Technology Letters*, vol. 20, no. 4, pp. 236-240, Jan. 1999.

[5] E. R. Brown, "RF-MEMS switches for reconfigurable integrated circuits," *IEEE Transactions on Microwave Theory and Techniques,* vol. 46, no. 11, pp. 1868-1880, Nov. 1998.

[6] C. Jung-Chih, "MEMS RF devices for antenna applications," in *2000 Asia-Pacific Microwave Conference*, Dec. 3-6, 2000, pp. 895-898.

[7] H. Takasu, "Estimation of equivalent circuit parameters for a millimetre-wave GaAs PIN diode switch," *IEE Proceedings on Circuits, Devices and Systems*, vol.150, no.2, pp. 92-94, Apr. 2003.

[8] C. J. Panagamuwa, A. Chauraya, and J. C. Vardaxoglou, "Frequency and beam reconfigurable antenna using photoconducting switches," *IEEE Transactions on Antennas and Propagation,* vol. 54, no. 2, pp. 449-454, Feb. 2006.

[9] N. Symeon, R. Bairavasubramanian, C. Lugo, Jr., I. Carrasquillo, D. C. Thompson, G. E. Ponchak, J. Papapolymerou, and M. M. Tentzeris, "Pattern and frequency reconfigurable annular slot antenna using PIN diodes," *IEEE Transactions on Antennas and Propagation,* vol. 54, no. 2, pp. 439-448, Feb. 2006.

[10] A. Guennou, B. Della, P. Queffelec, P. Gelin, and J. L. Mattei, "Influence of the magnetic field nonuniformity on an X-band microstrip Y-junction circulator bandwidth: theory/experiment comparison," *IEEE Transactions on Magnetics,* vol. 43, no. 6, pp. 2642-2644, Jun. 2007.

[11] G. H. Huff, "Electromagnetically functionalized colloidal dispersions and microfluidic reconfiguration mechanisms for phase-reconfigurable reflectarray elements," in *Proc. of 2008 URSI General Assembly*, Chicago, IL, Aug. 7-16, 2008.

[12] G. H. Huff, P. Bahukudumbi, W. N. Everett, A. Beskok, M. A. Bevan, D. Lagoudas, Z. Ounaies, "Microfluidic reconfiguration of antennas," in *Proc. of 2007 Antenna Applications Symposium*, Monticello, IL., Sept. 18-20, 2007, pp. 241 – 258.

[13] S. Goldberger and G. H. Huff, "Frequency reconfiguration of a microstrip patch antenna enabled by colloidal dispersions," in *Proc. of 2008 URSI North American Radio Science Meeting*, Boulder, CO, Jan. 3-6, 2008.

[14] S. A. Long and G. H. Huff, "A study of microfluidic compensation mechanisms for deformable antennas," in *Proc. of 2008 URSI General Assembly*, Chicago, IL, Aug. 7-16, 2008.

[15] P. Bahukudumbi, W. N. Everett, A. Beskok, M. A. Bevan, G. H. Huff, D. Lagoudas, and Z. Ounaies, "Colloidal microstructures, transport, and impedance properties within interfacial microelectrodes," *Applied Physics Letters*, vol. 90, no. 22, pp. 224102-1 – 224102-3, May 2007.

[16] J. McDonald and G. H. Huff, "Microfluidic mechanisms for reconfigurable dielectric resonator antennas," in *Proc. of 2008 URSI General Assembly*, Chicago, IL, Aug. 7-16, 2008.

[17] S. Goldberger, F. Drummond, R. Anderson, J. Barrera, A. Bolon, et al., "Small array behavior of frequency reconfigurable antennas enabled by functionalized dispersions of colloidal materials," in *Proc. of 2009 URSI North American Radio Science Meeting*, Boulder, CO, Jan. 5-8, 2009.

[18] D. Vincent, L. Jorat, and G. Noyel, "A simple reflection/transmission method for study of dielectric and magnetic liquids in the frequency range 0.1-20 GHz," in *12th International Conference on Conduction and Breakdown in Dielectric Liquids*, Jul. 15-19, 1996, pp.465-467.

[19] J. Obrzut and A. Anopchenko, "Input impedance of a coaxial line terminated with a complex gap capacitance - numerical and experimental analysis," *IEEE Transactions on Instrumentation and Measurement*, vol. 53, no. 4, pp. 1197-1201, Aug. 2004.

[20] S. Mikuteit, H. T. Buscher, R. M. McIntyre, "An artificial dielectric liquid phase shifter," in *Proc. of European Microwave Conference*, vol.2, Oct. 1971, pp.1-4.

[21] H. T. Buscher, R. M. McIntyre, and S. Mikuteit, “Variable-permittivity artificial dielectrics,” in *GMTT International Microwave Symposium Digest*, vol. 71, May 1971, pp. 192 – 194.

[22] Y. Kosta, and S. Kosta, “Liquid antenna systems,” in *Proc. of IEEE Antennas and Propagation Society International Symposium*, vol. 3, Jun. 20-25, 2004, pp. 2392 – 2395.

[23] H. T. Buscher, “Electrically controllable liquid artificial dielectric media,” *IEEE Transactions on Microwave Theory and Techniques*, vol. 27, no. 5, pp. 540 – 545, May 1979.

[24] Dow Corning Corp., Sylgard© 184 Silicone Elastomer Kit, Midland, MI.

[25] D. Piazza, N. J. Kirsch, A. Forenza, R. W. Heath, and K. R. Dandekar, "Design and evaluation of a reconfigurable antenna array for MIMO systems," *IEEE Transactions on Antennas and Propagation,* vol. 56, no. 3, pp. 869-881, Mar. 2008.

[26] R. N. Simons, C. Donghoon, and L. P. B. Katehi, "Microelectromechanical systems (MEMS) actuators for antenna reconfigurability," in *2001 IEEE MTT-S International Microwave Symposium Digest,* May 20-25, 2001, vol.1, pp.215-218.

[27] W. H. Weedon, W. J. Payne, and G. M. Rebeiz, "MEMS-switched reconfigurable antennas," in *IEEE Antennas and Propagation Society International Symposium*, vol.3, Jul. 8-13, 2001, pp.654-657.

[28] P. Panaia, C. Luxey, G. Jacquemod, R. Staraj, G. Kossiavas, L. Dussopt, F. Vacherand, and C. Billard, "MEMS-based reconfigurable antennas," *IEEE International Symposium on Industrial Electronics*, vol.1, May 4-7, 2004, pp. 175-179.

[29] A. H. M. Z. Alam, M. R. Islam, S. Khan, A. B. M. Nat, and M. M. B. A. Razak, "MEMS switch material dependency on designing a reconfigurable antenna," *IEEE International Conference on Semiconductor Electronics,* Oct. 29 -Dec. 1, 2006, pp.334-338.

[30] G. H. Huff and J. T. Bernhard, "Integration of packaged RF MEMS switches with radiation pattern reconfigurable square spiral microstrip antennas," *IEEE Transactions on Antennas and Propagation,* vol. 54, no. 2, pp. 464-469, Feb. 2006.

[31] E. Erdil, K. Topalli, M. Unlu, O. A. Civi, and T. Akin, "Frequency tunable microstrip patch antenna using RF MEMS technology," *IEEE Transactions on Antennas and Propagation,* vol. 55, no. 4, pp. 1193-1196, Apr. 2007.

[32] N. Haridas, A. T. Erdogan, T. Arslan, A. J. Walton, S. Smith, et al., "Reconfigurable MEMS antennas," *AHS '08 NASA/ESA Conference on Adaptive Hardware and Systems*, Jun. 22-25, 2008, pp.147-154.

[33] K. Van Caekenberghe and K. Sarabandi, "A 2-bit Ka-band RF MEMS frequency tunable slot antenna," *IEEE Antennas and Wireless Propagation Letters,* vol. 7, pp. 179-182, 2008.

[34] J. Kishor, P. Kumar, and A. K. Shrivastav, "Designing of varactor tuned microstrip patch antenna," *International Conference on Recent Advances in Microwave Theory and Applications*, Nov. 21-24, 2008, pp.907-909.

[35] G.-M. Yang, X. Xing, A. Daigle, M. Liu, O. Obi, et al., "Electronically tunable miniaturized antennas on magnetoelectric substrates with enhanced performance," *IEEE Transactions on Magnetics*, vol. 44, no. 11, pp. 3091-3094, Nov. 2008.

[36] M. Al Ahmad, L. Young Taek, C. Chae Il, Y. Eui-Jung, and R. Plana, "Tunable (LSMO) ferromagnetic thin films for radio frequency applications," *IEEE Microwave and Wireless Components Letters,* vol. 19, no. 1, pp. 36-38, Jan. 2009.

[37] S. Zhang, G. H. Huff, J. Feng, and J. T. Bernhard, "A pattern reconfigurable microstrip parasitic array," *IEEE Transactions on Antennas and Propagation,* vol. 52, no. 10, pp. 2773-2776, Oct. 2004.

[38] K. Boyon, P. Bo, S. Nikolaou, K. Young-Sik, J. Papapolymerou, and M. M. Tentzeris, "A novel single-feed circular microstrip antenna with reconfigurable polarization capability," *IEEE Transactions on Antennas and Propagation,* vol. 56, no. 3, pp. 630-638, Mar. 2008.

[39] C. Rui-Hung and J. S. Row, "Single-fed microstrip patch antenna with switchable polarization," *IEEE Transactions on Antennas and Propagation,* vol. 56, no. 4, pp. 922-926, Apr. 2008.

[40] M. S. Silberberg, *Chemistry The Molecular Nature of Matter and Change*, 2nd ed., K. T. Kane, Ed. Boston: McGraw Hill, 2000.

[41] A. Sihvola, *Electromagnetic Mixing Formulas and Applications*, 1st ed., P. J. B. Clarricoats and E. V. Jull, Eds. Padstow, Cornwell, England: The Institution of Electrical Engineers, 1999.

[42] WD-40, 3in1 Oil©, San Diego, CA.

[43] TPL, Inc., NanOxide™ HBS 1000 Barium Strontium Titanate Powder, Albuquerque, NM.

[44] P. Leddy. Material Data Safety Sheet. FerrMag Technologies, Inc., Edison, NJ, Available: http://www.fermagtechnologies.com/MSDS.html

[45] TPL, Inc., Nanosperse™ 484 Wetting & Dispersion, Albuquerque, NM.

[46] C. A. Balanis, *Antenna Theory: Analysis and Design*, Third ed. Hoboken: John Wiley & Sons, Inc., 2005.

[47] F. Jia-Shiang, X. A. Zhu, J. D. Phillips, and A. Mortazawi, "A ferroelectric-based impedance tuner for adaptive matching applications," *IEEE MTT-S International Microwave Symposium Digest*, Jun. 15-20, 2008, pp.955-958.

[48] R. E. Collin, *Foundations for Microwave Engineering*, 2th ed., D. G. Dudley, Ed. New York: John Wiley & Sons, Inc., 2001.

[49] N. Marcuvitz, Waveguide Handbook. New York: McGraw-Hill Book Company, 1951.

[50] C. A. Balanis, *Advanced Engineering Electromagnetics*, 17th ed. Hoboken: John Wiley & Sons, Inc., 1989.

[51] Ansoft, HFSS© v11.1, Pittsburgh, PA 15219

[52] R. F. Harrington, *Time-Harmonic Electromagnetic Fields*, 4th ed., D. G. Dudley, Ed. New York: Wiley-Interscience, 2001.

[53] P. M. Nikolic and L. D. Zivanov, "Dielectric properties of strontium hexaferrite in microwave, infrared and far infrared ranges," *Fifth International Conference on Dielectric Materials, Measurements and Applications*, Jun. 27-30, 1988, pp.332-335.

[54] A. Korolev, L. Subramanian, and M. Afsar, “Complex permittivity and permeability of strontium ferrites at millimeter waves,” *J. Appl. Phys.*, vol. 99, no. 8, pp. 08F504-1 - 08F504-3, Apr. 2006.

[55] T. Nicolas, C. Philippe, S. Ronan, S. Vincent, and F. Hiroyuki, "Polydimethylsiloxane membranes for millimeter-wave planar ultra flexible antennas," *Journal of Micromechanics and Microengineering*, vol. 16, no. 11, pp. 2389-2395, Nov. 2006.

[56] R. Garg, P. Bhartia, I. Bahl, and A. Ittipiboon, *Microstrip Antenna Design Handbook*, 1st ed. Boston: Artech House, Inc., 2001.

[57] National Instruments, Labview© v8.6, Austin, TX 78759

APPENDIX

Matlab Code for COSMIX Analytical Model

```
clc; close all; clear all;
%*****************************************
%Change the following values
%*****************************************
a=0.00127/2; %Radius of inner conductor in m
b=0.0041/2; %Radius of dielectric in m
d=0.00022; %Space gap at end of coax line in m
q=0.00075; %Radius of the inlet/outlet in m
length=0.0100/3; %Length of SMA probe in m
length2=0.00758; %Length of T. L. in m
c=3.0e8; %Speed of light in m
f=0.4e9:0.4e9:1.6e9;
%f=0.35e9:0.001e9:3.0e9; %Frequency in GHz
e0=10^(-9)/(36*pi);%F/m
u0=4*pi*10^(-7);%H/m
er_uk=11.4; %Dielectric value of unknown material
er=2.1; %Dielectric constant of T. L.
ur_uk=1; %Permiability of unknown material
ur=1; %Permiability of T. L.
xmn=2.4049; %Zero of Bessel function for TM01
%*****************************************
%Change the following values for lossy case only
%*****************************************
loss_tangent=0.001;
loss_tangent_uk=0.0045;
sigma=4.098*10^7; %Conductivity of T. L. Gold metal
%*****************************************

[lambda,w]=wave_length(c,f);
[lambda_g]=guided_wave_length(lambda, ur_uk, er_uk);

[ec]=complex_permittivity(e0,er,loss_tangent);%Complex dielectric
constant of T. L.
[ec_uk]=complex_permittivity(e0,er_uk,loss_tangent_uk);%Complex
dielectric constant of unknown material

sigma_x=(loss_tangent_uk*er_uk*e0*w)./2.;

[L]=self_inductance(ur,u0,a,b);
[Lx]=self_inductance(ur_uk,u0,a,b);
[C]=shunt_capacitance(er,e0,a,b);
[Cx]=shunt_capacitance(er_uk,e0,a,b);
[R]=conductor_resistance(f,ur,u0,a,b,sigma);
[Rx]=conductor_resistance(f,ur_uk,u0,a,b,sigma);
[G]=shunt_conductance(ec,a,b,w);
[Gx]=shunt_conductance(ec_uk,a,b,w);
```

```
%Propagation constant
[prop_x]=prop_const(Lx,Cx,Rx,Gx,w);
[prop]=prop_const(L,C,R,G,w);

%Characteristic impedance of transmission line with variable dielectric
[Zx,Yx]=tl_impedance(Lx,Cx,Rx,Gx,w);
%Characteristic impedance of transmission line
[Z0,Y0]=tl_impedance(L,C,R,G,w);

%Capacitance of the gap
[Z_t]=marcuvitz_gap_capacitance(a,b,d,lambda_g,Yx);
s=sqrt(b.^2.+d.^2.);
A=pi*b.*s+pi*b.^2.; %Cross sectional area of gap
G_t=(sigma_x*A)./d; %Conductance of gap

%Cut off frequency of Circular waveguide TM
[fc]=cutoff_freq_TM(q,ur_uk,er_uk,u0,e0,xmn);
%Attenuated Capacitance of a circular waveguide operating in TM mode
[Z_wave_TM]=TM_CWG_capacitance(fc,f,ur_uk,u0,er_uk,e0);

%Region 1
Z=1./(1./Z_t+G_t);
%Region 2
[gamma]=reflection_coef_load(Z,Zx);
[gamma2]=reflection_coef_line(prop_x,gamma,length);
[Z2]=impedance_from_gamma(gamma2,Zx);
%Region 3
Z3=1./(1./Z2+1./Z_wave_TM);
%Region 4
[gamma3]=reflection_coef_load(Z3,Zx);
[gamma4]=reflection_coef_line(prop_x,gamma3,length);
[Z4]=impedance_from_gamma(gamma4,Zx);
%Region 5
Z5=1./(1./Z4+1./Z_wave_TM);
%Region 6
[gamma5]=reflection_coef_load(Z5,Zx);
[gamma6]=reflection_coef_line(prop_x,gamma5,length);
[Z6]=impedance_from_gamma(gamma6,Zx);
%Region 7
[gamma7]=reflection_coef_load(Z6,Z0);
[gamma8]=reflection_coef_line(prop,gamma7,length2);
[Z7]=impedance_from_gamma(gamma8,Z0);
%Region 8
[gamma9]=reflection_coef_load(Z7,Z0);

%S-Parameter calculation for S11
[mag_S11, ph_S11]=scattering_11(gamma7)
%figure(1);
%plot(f, ph_S11)
%figure(2);
%plot(f, mag_S11)
phase=rot90(ph_S11);
mag=rot90(mag_S11);
save('C:\smith2','mag','phase','-ASCII','-DOUBLE', '-TABS')
```

VITA

Sean Arthur Goldberger
sagoldbe@neo.tamu.edu

3128 TAMU, 214 Zachry Bldg.
College Station, TX 77843

Professional Preparation

M.S., Electrical Engineering, Texas A&M University, College Station, TX, May 2009

B.S., Electrical Engineering, University of Colorado, Denver, CO, May 2006

Appointments and Research Experience

Graduate Mentor, Space Engineering Institute, Texas A&M University, College Station, TX, 2008-Present

Graduate Adviser, Aggie Sat, Department of Aerospace Engineering, Texas A&M University, College Station, TX, 2008-Present

Lab Manager, Wireless Communications Lab, Electrical and Computer Engineering Department, Texas A&M University, College Station, TX, 2008-Present

Teaching Assistant, Electrical and Computer Engineering Department, Texas A&M University, College Station, TX, Spring 2008

Publications and Conferences (* = presenter)

[1] S. Goldberger* and G. H. Huff, "Frequency reconfiguration of a microstrip patch antenna enabled by colloidal dispersions," in *Proc. of 2008 URSI North American Radio Science Meeting*, Boulder, CO, Jan. 3-6, 2008.

[2] G. H. Huff*, S. Goldberger, and S. A. Long, "The RF cuttlefish: Overview of biologically inspired concepts for reconfigurable antennas and smart skins" in *Proc. of 2008 Antenna Applicat. Symp.*, Monticello, IL., Sept. 16-18, 2008, pp. 291-305.

[3] S. Goldberger*, F. Drummond, R. Anderson, J. Barrera, A. Bolon, et al., "Small array behavior of frequency reconfigurable antennas enabled by functionalized dispersions of colloidal materials," in *Proc. of 2009 URSI North American Radio Science Meeting*, Boulder, CO, Jan. 5-8, 2009.

[4] S. Goldberger*, F. Drummond, R. Anderson, J. Barrera, A. Bolon, et al., "Small array behavior of frequency reconfigurable antennas enabled by functionalized dispersions of colloidal materials," in *Proc. of 2009 URSI/IEEE Antennas and Propagation Society Meeting*, Charleston, SC, Jun. 1-5, 2009.

[5] S. Goldberger*, F. Drummond, R. Anderson, J. Barrera, A. Bolon, et al., "Frequency reconfiguration of a small array enabled by functionalized dispersions of colloidal material," in *Proc. of 2009 AIAA/USU Small Satellites Elements of New Space Systems*, Logan, UT, Aug. 10-13, 2009.